UNIVERSITY OF CALIFORNIA
IRVINE

Radiative Cooling Strategies by Bio-Inspired Nanowire Trees

THESIS

submitted in partial satisfaction of the requirements
for the degree of

MASTER OF SCIENCE

in Mechanical and Aerospace Engineering

by

Anirudh Krishna

Thesis Committee:
Professor Jaeho Lee, Chair
Professor Derek Dunn-Rankin
Professor Timothy Rupert

2016

DEDICATION

To
My parents

and
The people who left a mark in my life

TABLE OF CONTENTS

LIST OF FIGURES

NOMENCLATURE

λ	Wavelength
d	Spacing between adjacent layers
A	Surface area
T	Temperature
ε	Surface emissivity
$\varepsilon_{n\lambda}$	Normal spectral emissivity
ε_r	Rough surface emissivity
ρ_r	Rough surface reflectivity
ρ_p	Polished surface reflectivity
α	Absorptivity
n	Refractive index
κ	Extinction coefficient
ρ	Electrical resistivity
p	Specularity/asperity
θ	Angle of incidence/emission
θ_i	Incident angle
θ_s	Scattered angle
Ω_i	Solid angle of incidence
Ω_s	Solid angle of scattering
p	Tangent of angle between incident field and incident angle
$P(p)$	Probability of event occurring at a given p
σ	Surface roughness
σ_l	lamella spacing

σ_h	Average ridge height
z-z_m	Deviation of surface height from mean
P	Radiative power
P_{BB}	Blackbody radiative power
P_{rad}	Radiative power from surface
P_{atm}	Radiative transfer through atmosphere
P_{sun}	Solar radiative power
$P_{cond+conv}$	Power from conduction and convection
ϕ	Radiative power flux
h_c	Convective heat transfer coefficient

CONSTANTS

h	Planck's constant	6.626×10^{-34} J·s
c	Speed of light	2.998×10^{8} m/s
k_B	Boltzmann constant	1.381×10^{-23} J/K
σ	Stefan-Boltzmann constant	5.670×10^{-8} W/m^2·K^4

ACKNOWLEDGMENTS

I would like to express my sincere gratitude to my advisor, Dr. Jaeho Lee, for his invaluable mentorship, guidance and support, which helped my advance my knowledge and research aptitude in a motivated and scholarly manner. His eagerness to counsel and mentor were integral to my academic progress at the University of California, Irvine. My interactions with him, through individual meetings, lab meetings and otherwise, lay at the foundation of who I aim to be as a researcher and scholar.

I am also extremely grateful to, and indebted to, Dr. Derek Dunn-Rankin, who was an excellent mentor to me in my first few months of graduate studies. His vast knowledge and know-how are qualities I will strive to emulate in my academic life.

I would also like to thank Dr. Timothy Rupert, whose support and counsel through the course of this study in his capacity as a thesis committee member aided greatly in shaping the study to what it presently is. I am thankful for his practical suggestions and comments, which stem from his fondness for knowledge. Attending his classes will always be part of the moments I cherish in graduate life.

I thank all the members of the Nano Thermal Energy Research group, whose unquestioning help paved the way for a smooth transition from incubation of an idea to the thesis and study as it is presented. These are the people who showed me that spending time at the lab could be more fun than I thought.

I am very thankful to the people in my life, without whom none of this would have been possible, foremost to my parents, whose unwavering support and unconditional love is the basis of who I am, where I am and what I am. My academic pursuits are made possible due to their intentions of placing prime importance on education, regardless of financial or other hurdles. This thesis, and all of my academic work, is a dedication to their love.

ABSTRACT OF THE THESIS

Radiative Cooling Strategies by Bio-Inspired Nanowire Trees

By

Anirudh Krishna

Master of Science in Mechanical and Aerospace Engineering

University of California, Irvine, 2016

Professor Jaeho Lee, Chair

Spectral thermal radiation properties play a vital role in governing heating and cooling phenomena on surfaces, especially those exposed to the sun in the ambient environment. The wavelength of incident solar radiation responsible for surface heating typically ranges from 200 nm to 2500 nm. Radiative cooling, by means of utilizing the coldness of outer space (~2.7 K), presents a possible solution of avoiding undesirable heat generation. The atmospheric transmission window, which enables radiative cooling in the ambient environment, ranges from 8 μm to 14 μm to reemit incident radiation to outer space. Effective utilization of radiative cooling involves controlling the surface emissivity spectrum, thereby governing the thermal energy exchange. Here, we propose a novel emissivity control technique based on nanowire tree structures that are inspired by the unique colorization of *Morpho* butterflies. The proposal offers the design of the nanowire tree aided by computational methods which show that the nanowire tree keeps the emissivity below 0.1 in the spectral range between 1 μm and 6 μm, which minimizes solar heating, while keeping the emissivity above 0.8 in the range beyond 8 μm, which maximizes the cooling opportunity in the ambient environment. This enables a near 6°C temperature

reduction with respect to the ambient, which is substantially lower than bare surfaces of common engineering materials (e.g. 90% lower than Al_2O_3). The nanowire trees offer multi-dimensional geometric variations for enhanced tunability of emissivity, providing a significant breakthrough in thermal management methods.

INTRODUCTION

Effects of Incident Radiation on Exposed Surfaces

Radiation is a combination of various wavelengths ranging from the ultraviolet and X-ray regions (with very low wavelengths down to roughly 300 nm), extending to the infrared and far infrared (with wavelengths starting at roughly 1 μm and going upwards), covering the visible region of light (roughly 300 nm to 700 nm) in between. Surfaces exposed to radiation of different wavelengths exhibit a vast array of spectral properties, ranging from optical properties such as refractive index, reflectance, transmittance and absorbance, to mechanical properties such as specularity and surface transport phenomena.

The solar radiation is governed by Planck's law of radiation based on the solar surface temperature (which is around 5,800 K), with the radiation based on atmospheric windows for their radiation or transmission [1][2]. This leads to the incident solar radiation on the earth falling with its majority in the visible or infrared regions of the spectrum.

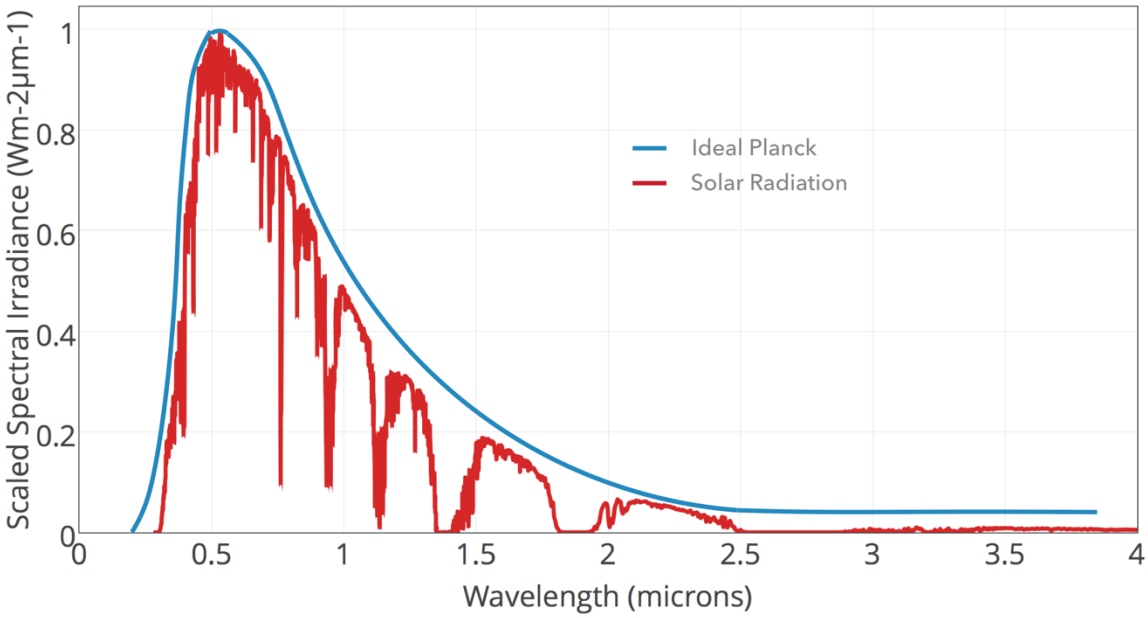

Figure 1. Incident solar radiation on the surface of the earth (and all terrestrial surfaces), depicted as a function of spectral irradiance with wavelength. The aim of thermal management is to reduce the spectral emissivity for the range of wavelengths showing a peak in solar radiation. The curve shown is a result of the classic Planck radiation curve at the solar surface temperature, with the interaction of the earth's atmosphere, and the atmospheric transmission windows [1][2].

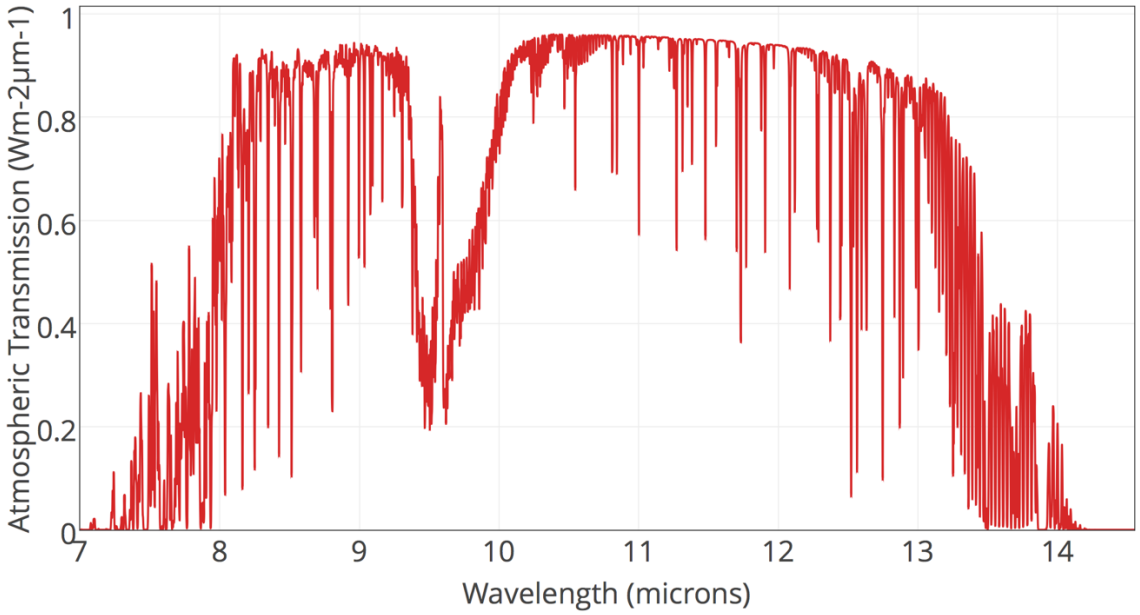

Figure 2. Atmospheric transmission window for the earth [2], ranging from roughly 8 to 13 microns, allowing for effective reemission of incident radiation back into outer space. The aim for thermal management is to increase the emissivity for the spectral range shown here.

Heat is a measure of average energy possessed by the sample at an atomic/molecular level, requiring an absorption of energy for an increase in heat. All incident radiation consists of energetic photons, and they can therefore heat a surface up if they are absorbed into the material. However, with varying quantum mechanical properties of different types of matter, certain frequencies of radiation may transfer energy directly, through resonance, to increase vibration, bond bending, or electron transitions to the substance it interacts with. In this aspect, infrared radiation is strongly absorbed by many types of molecules, increasing the vibration or bending of chemical bonds, and therefore increasing the heat. Therefore, infrared radiation increases the heat of most surfaces it is incident on.

Surface Thermal Management

Surface heat generation can govern the performance of devices associated with the surface, prominently in the field of power generation, and in civilian areas, such as the heating of buildings, automobiles and other consumer devices and applications. Eliminating the heating effect of the incident radiation would lead to better performance of the surfaces, as this avoids deterioration of material properties with an increase in surface temperature, or even general failure of components or materials. This makes it imperative to understand the underlying physics of the problem in order to effectively address it.

Conventional methods to reduce the adverse effects of the generated heat involve the use of either excessive power/energy [3-5], or barring that, other less efficient means of thermal management and surface property control. This ultimately places financial and

energy burdens, or other user discomfort, towards cooling the surface. While such conventional means have failed to arrive at an acceptable solution, novel solutions have been proposed [6-11], which make use of inherent surface properties to control the surface temperature, with some of them even using the extremely low temperature of outer space as a heat sink for hot surfaces. The aim, now, is a perfection of the methods proposed, and the work presented here offers a bio-inspired means to aid in this.

Outline of Research

Chapter 1 identifies the existing thermal management methods with a literature review on both active surface cooling and passive surface cooling, and introduces the concept of radiative cooling. Chapter 2 presents a novel thermal management solution that derives its inspiration from nature, specifically the *Morpho* butterfly and its unique optical properties. Chapter 3 defines the surface emissivity, thermal and optical properties of any given surface, and explains the factors of dependence of surface emissivity, and measurement techniques. Chapter 4 details the modeling technique used in this study and its mathematical formulation, and provides the computational results of the modeled bio-inspired nanowire trees. Chapter 5 presents computational results of the thermal analysis of the nanowire trees, showing a conversion of the emissivity to the surface temperature. Chapter 6 lists the current limitations of the study presented here, and details the scope of future work. Finally, Chapter 7 offers concluding remarks on the bio-inspired solution proposed this study, and its implications for breakthroughs in thermal management.

CHAPTER 1: LITERATURE SURVEY

In this chapter, existing solutions to surface thermal management are identified, and their potential viability for the study are discussed, with an aim to alleviate the drawbacks and utilize effective means to enhance the present study.

1.1 Active Surface Cooling

One of the most pervasive techniques of surface temperature control is active surface cooling, which is defined as a system that utilizes energy to cool the surface. Active surface cooling is a broad category that encompasses heat exchangers, cooling fans, refrigeration and other such methods.

Al-Amri and Mallick [3] present one such method for the alleviation of the operation temperature of a solar cell by using air flow to cool the set-up. The consideration of solar cells is analytically equivalent to any terrestrial surface exposed to incident solar radiation, and thus aids the present study. The schematic of the set-up is shown in Fig. 3.

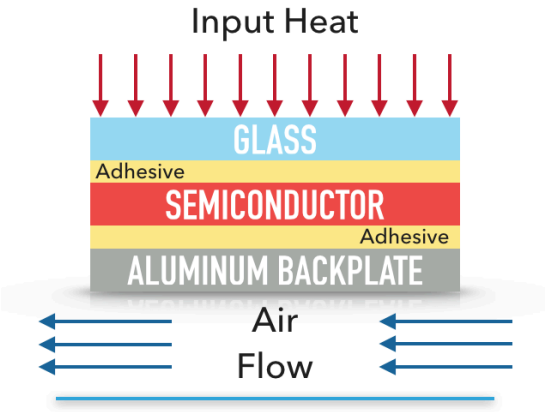

Figure 3. Schematic of air-based active cooling system proposed by Al-Amri and Mallick [3], with the solar cell sandwiched between a glass plate and an aluminum back plate. The air flow through the bottom of the set-up aids in convective heat transfer away from the device.

The flow of air helped carry the heat away from the solar cell, thus cooling it. Such an apparatus, however, depends on a variety of factors, including the air inlet velocity, channel width and the effectiveness of convective heat transfer [3].

Another perspective to addressing the problem of solar cell heating was offered by Najafi and Woodbury [4], who make use of the Peltier effect. The Peltier effect, or the Bridgman effect is a thermoelectric effect where passing an electric current through an anisotropic crystal leads to a cooling or heating effect. The schematic for the set-up is shown in Fig. 4.

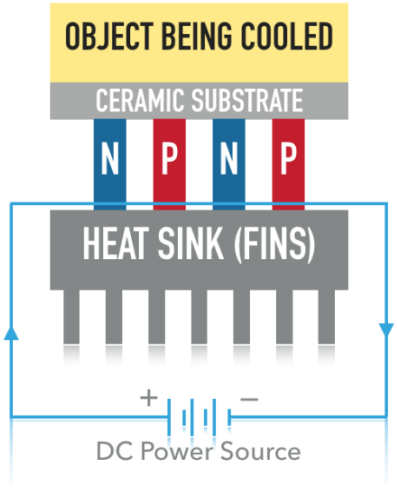

Figure 4. Schematic of thermoelectric effect (Peltier effect) based active cooling system proposed by Najafi and Woodbury [4]. An electric current through the substrate aids in cooling of the object, further aided by the use of fins.

Careful selection of the substrate beneath the object being cooled is necessary, as the Peltier cooling of the object depends upon the anisotropy of the substrate. An anisotropic crystal shows non-uniform charge flow during the passing of an electric current, thus leading to a temperature gradient. Such a set-up depends heavily upon the

substrate being used, and even so does not prove to be as efficient as other conventional active cooling systems. This is evidenced by the results, which suggest that the operation of the Peltier cooler for effective cooling of the PV cell being cooled, requires usage of the power produced by the cell itself [4], proving impractical for actual use as yet.

Moharram *et al.* [5] have offered an enhancement of a conventional active cooling system to assist in alleviating its drawbacks. Water spray cooling is another means of cooling the surfaces of photovoltaic (PV) cells, that makes use of the spraying of water and the consequential flow to help in the convective cooling of the solar cell surface, as shown in Fig. 5.

Figure 5. PV cells shown in use, with water cooling system attached on the top end of the set-up. Spraying of water on the surface of the cells helps cool them. (image courtesy: Dominic Alves)

While analysis of the water cooling system offers possible suggestions for optimization of surface cooling with resource usage, large scale operation as yet involves vast quantities of water and power being consumed.

Analysis by Florides *et al.* [12] provides a comprehensive picture of the socioeconomic impact of the use of active cooling systems, stating that the use of active cooling systems in buildings has high capital costs for subpar to par coefficient of

performance. This tends to have a high impact especially in arid regions, with unpredictable resource availability.

1.2 Passive Surface Cooling/Radiative Cooling

Passive cooling methods can eliminate the power consumption and the financial burden required by active cooling. Various means of passive cooling have been demonstrated based on improved conduction and radiation mechanisms, mainly by facilitating the distribution of heat over the surface of the sample, to improve radiative or conductive cooling. Applications and examples of such passive cooling methods include but are not limited to the use of metallic nanowire coatings by Hsu *et al*. [6] and metamaterials by Liu *et al*. [7], as shown in Fig. 6.

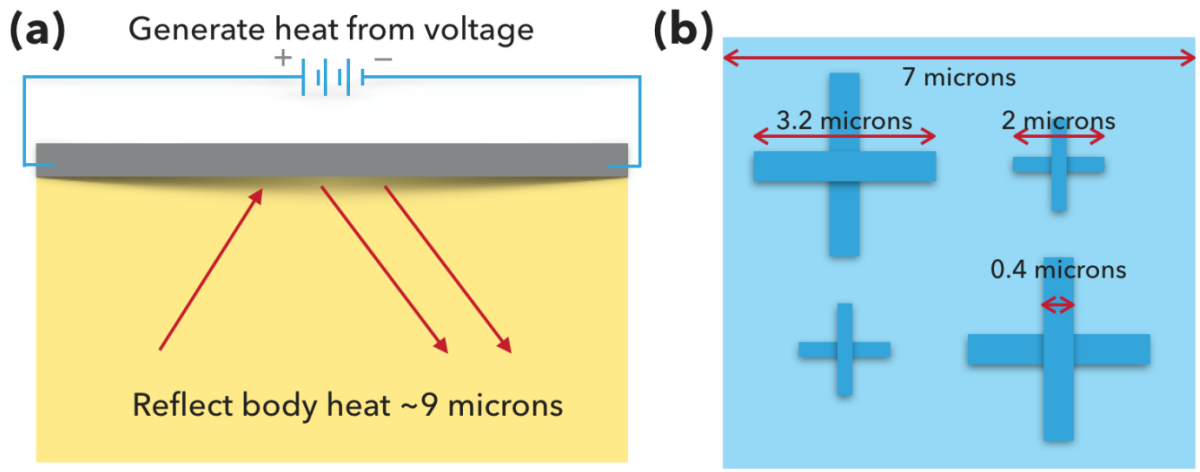

Figure 6. (a) Schematic of metallic nanowire (AgNW) coating used for personal thermal management, as proposed by Hsu *et al.* [6]. (b) Schematic of metamaterial used for surface temperature control proposed by Liu *et al.* [7].

Radiative cooling, a means of passive cooling, involves the use of the atmospheric transmission window to reemit the incident radiation selectively in the thermal

wavelengths. The atmospheric transmission window between 8 and 14 microns allows for relatively unhindered reemission of radiation from the surface of any terrestrial object, back out of the earth's atmosphere [2], where the cold temperatures of outer space (around 2.7 K) would act as a heat sink to receive the reemitted heat from the object. Zhu *et al*. [8] have demonstrated the use of the coldness of the universe as a heat sink for passive radiative cooling of solar cells. The reemission characteristics would need to be tailored to pass through the atmospheric transmission window of roughly 8 to 14 microns wavelength [13], and the surface would consequently need high emissivity characteristics for this wavelength window to facilitate effective reemission.

Rephaeli *et al*. [9] suggested the use of photonic structures to tackle the spectrally selective emissivity characteristics required for passive radiative cooling. Expanding on the idea, the emissivity profile of microscale periodic pyramids of silica, as investigated by Zhu *et al*. [10], attains high values for the spectral emissivity beyond 6 microns. Further enhancement of the use of periodic micro/nanoscale photonic structures for emissivity controlled radiative cooling could be achieved by more closely tailoring the emissivity profile to the infrared window. This was demonstrated by Raman *et al*. [11], as shown in Fig. 7, using the same principle.

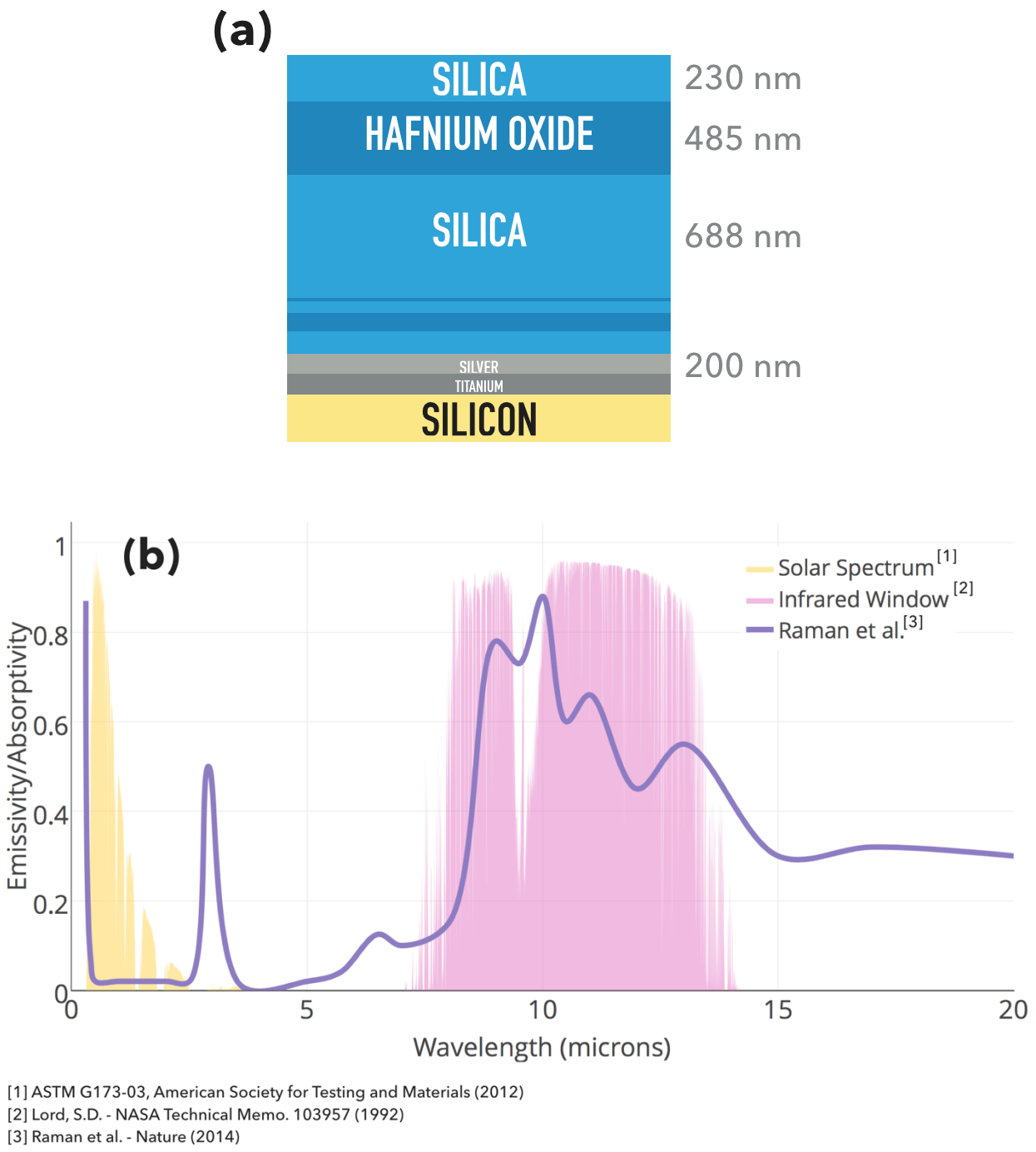

Figure 7. (a) Schematic of the multilayer photonic cooler proposed by Raman *et al.* [10]. (b) Emissivity spectrum of the photonic cooler, showing low emissivity for most wavelengths, except within the atmospheric transmission window, allowing for effective reemission of incident radiation.

The multilayer photonic cooler of Raman *et al*. shows an emissivity profile that rises at around 8 microns and falls at around 13-14 microns. However, this fall in emissivity is relatively small, as the reflectivity value still remains in the mid-range. This permits heating of the surface by incident radiation in the far infrared regions, which reduces a possible 1 to 3 Kelvin drop in surface temperature. Improvement in performance on this front would involve a more faithfully tailored emissivity spectrum, allowing for lower emissivity values as the wavelengths exit the atmospheric transmission window, permitting a higher temperature drop for the surface.

CHAPTER 2: BIO-INSPIRED STRATEGIES

While the performance of the photonic crystals and metamaterials used so far have yielded some spectral control of emissivity, a possible means to improve the results achieved so far would be to exploit the spectrally selective emissivity control characteristics of optically varying periodic structures such as those on the wings of the *Morpho* butterfly. The selection of the *Morpho* butterfly as a source of inspiration is based on the unique spectral characteristics of the structures on its wings. The wings of the *Morpho* butterfly have long been studied for an understanding of the source of their bright blue-violet color, as noted by Watanabe *et al*. [14]. This vivid coloration was inferred by Pris *et al.* [15] to be a result of spectrally selective reflectance. While it was initially thought to be a result of interference in a multilayer structure of chitin and air, later analyses have shown that it is a result of periodic nanostructures made of long rows of ridges (stems), with periodic lamellae (branches) on either side of the ridge, documented by Siddique *et al*. [16] and Yoshioka *et al.* [17] among others [14][18], as shown in Fig. 8. This discovery was significant because ir demonstrated that structural variations at the nanoscale can produce optical behaviors that would normally be ascribed to changes in material properties.

The generally accepted dimensions for a simplified simulation of the nanostructures are also gathered from Siddique et al. [16], with the ridges reaching an average height of around 1.25 microns, and the lamellae at the tips around 29 nm long. The lamellae alternate on either side of the ridge as we go down towards the base, and each alternating lamella is roughly 40-45 nm longer than the previous one, until we reach a maximum

lamella length of around 318 nm. Fig. 8(c) depicts the simulated approximate structure of the nanowire trees on the *Morpho* wing.

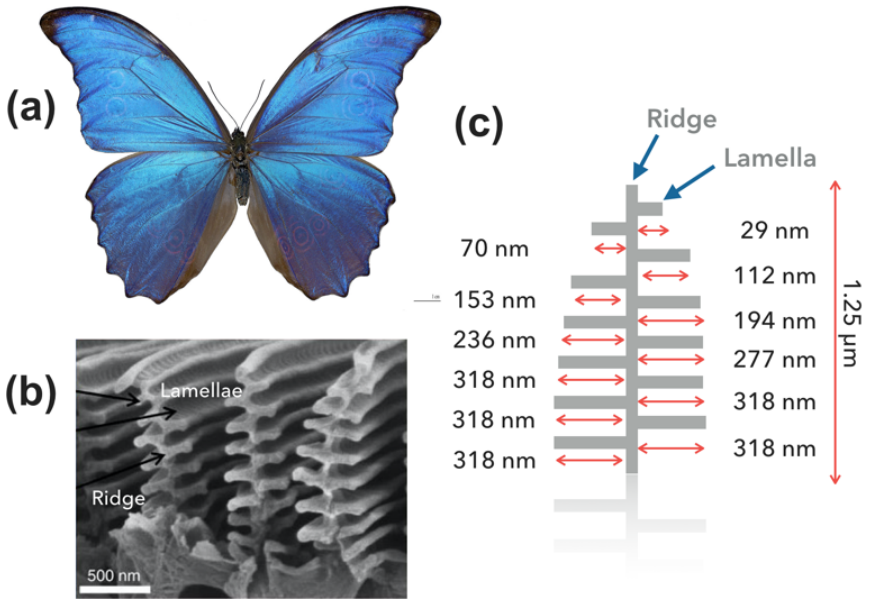

(a) Didier Descouens - Muséum de Toulouse (2011)
(b) Potyrailo et al. - Nature Communications (2014)

Figure 8. Topography of the nanostructures on a *Morpho* butterfly wing. (a) *Morpho* butterfly, with its vividly colored wings (image courtesy: Didier Descouens). (b) SEM image of the nanostructures present on the wings of the *Morpho* butterfly showing a central ridge, and branches of lamellae [20]. (c) Approximate dimensions (in nm) of the ridge-lamellae structures on the butterfly wing with data as detailed in Siddique *et al*. [16].

2.1 Optics of the Butterfly Wing

Butt *et al*. [19] supplement the structural analysis of the butterfly wing, stating that it is a combination of interference at the lamellae and ridges, diffraction at the surface, and incoherence that lead to the brilliant coloration of the wings of the butterfly. Preliminary analysis of the photophysics of the nanostructures of the *Morpho* wing by Kinoshita *et al*.

[18], reveals an explanation for the optical phenomena that control the structural coloration and reflectance spectrum of the *Morpho* butterfly.

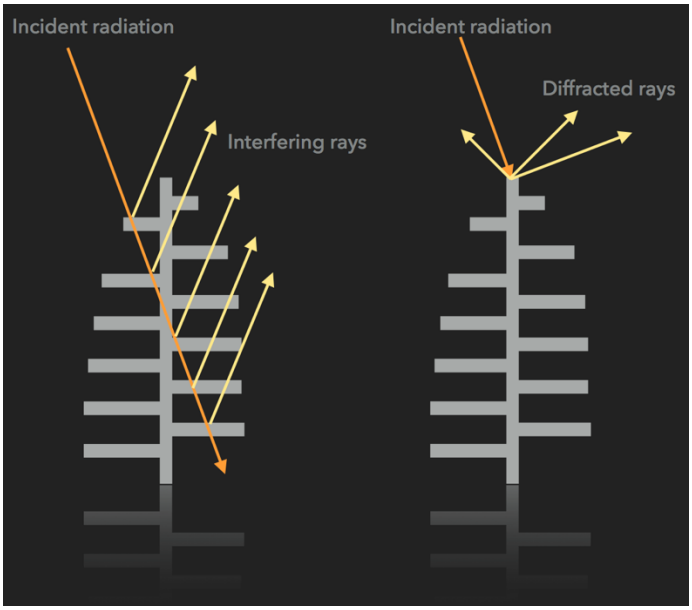

Figure 9. An explanation of the optical phenomena for the structures on the wings of the *Morpho* butterfly, depicting multilayer interference (left), and multilayer diffraction (right).

Considering the structures on the butterfly wing to be lamellae of a finite size, positioned separated from each other along the direction perpendicular to the ridges, as in most *Morpho* species (e.g. *M. didius*, *M. sulkowskyi* and *M. rhetenor*), it becomes apparent that the structure causes the diffraction of light in addition to the interference within a lamella. Moreover, assuming ridges of equal heights along any given cross section of the wing leads to an added level of interference arising from considering the spacing between the ridges as a source for multi-slit interference. Kinoshita et al. [18] suggest that this restricts the direction of light diffraction and causes diffraction spots. Random distribution of ridge heights in real life, however, limits the presence of such diffraction spots.

The study also analyzes the angular dependence of these optical phenomena, assuming that there is no effect of refraction or reflection on the incident radiation as it passes from one layer through the next. Alleviation of drawbacks from such an assumption involves considering the multilayer lamellae structures under Bragg diffraction, as shown in Eq. (1).

$$n\lambda = 2d \sin\theta \qquad (1)$$

The order of diffraction is denoted by n, with λ being the wavelength of incident radiation, d the spacing between each adjacent lamellae and θ the angle of incidence. For wide-angle diffraction, the angle of incidence approaches 90 degrees from the normal, leading to the sine of the angle to approach 1. A case where n is taken to be 1 leads to the approximate relation between lamellae spacing and incident wavelength as shown in Eq. (2). This spectral selectivity corresponds to a high reflectivity value for certain wavelengths.

$$\lambda = 2d \quad OR \quad d = \lambda/2 \qquad (2)$$

Another observance is that the light diffracted by each layer interferes in the far-field region. Although this assumption does not account for multiple reflection, it still holds the physical essence of the structural coloration and the background optics of the butterfly wing nanostructures. The derivation of the optical basis for the phenomena by Kinoshita *et al.* [18] corresponds to the first-order solution of the wave equation under the presence of complex dielectric materials.

Although many unique and interesting applications have been developed from this spectral-selective coloration of the *Morpho* butterfly wing and its high level of spectral tunability, as in the design of artificial thermal sensors and vapor sensors [20], a proposed

application of this spectral selectivity is to enhance the performance metrics of surfaces exposed to solar radiation.

CHAPTER 3: SURFACE EMISSIVITY

While the ideal scenario for radiation heat transfer assumes that the bodies involved follow Planck's law of radiation (at least as gray bodies), real bodies rarely behave so. If we consider the net radiated power from an ideal body following Planck's law, we arrive at Eq. (3), which is the Stefan-Boltzmann equation for such a body. Such ideal bodies are referred to as blackbodies.

$$P_{BB} = \sigma A T^4 \tag{3}$$

$$P = \varepsilon \sigma A T^4 \tag{4}$$

Here, P_{BB} is the radiative power emitted by the blackbody, σ is the Stefan-Boltzmann constant (5.67×10^{-8} W/m^{2}K^4), ε is the surface emissivity, A is the area under consideration and T is the temperature of the surface. The Stefan-Boltzmann equation for gray bodies is given in Eq. (4). Gray bodies follow the ideal blackbody Stefan-Boltzmann equation with a deviating factor, called the surface emissivity of the body. The emissivity is a property of the surface of a material, and is defined as its effectiveness in emitting energy as thermal radiation. Real bodies often have substantial spectral band behavior that deviates from the gray body assumption, but many materials can be considered spectrally gray for most thermal analyses. Quantitatively, emissivity is the ratio of the thermal radiation from a surface to the radiation from an ideal blackbody surface at the same temperature as given by the Stefan–Boltzmann law, shown in Eq. (5), and can vary in value from 0 to 1.

$$\varepsilon = \frac{P}{P_{BB}} \tag{5}$$

An emissivity value of 1 indicates an ideal radiator, with the surface being able to emit (or absorb, as absorptivity equals emissivity) all incident energy. Lower emissivity values progressively indicate worse emission characteristics, with 0 indicating no emission.

3.1 Factors of Dependence

Surface emissivity depends on a variety of factors, which in turn depend on the underlying surface characteristics. The most important factors of dependence of surface emissivity are the incident wavelength, inherent material characteristics, angle of incidence/emission of radiation, and surface roughness (specularity/asperity).

Autio and Scala [21] in their optical analysis of isotropic and anisotropic materials state the use of the empirical Hagen-Rubens relation for metals to compute the surface emissivity of the metal as a function of the incident or emitted wavelength. The relation, which makes use of the Drude theory, is shown in Eq. (6).

$$\varepsilon_{n\lambda} = 36.50\sqrt{\left(\frac{\rho}{\lambda}\right)} \qquad (6)$$

ρ gives the D.C. electrical resistivity in Ωcm, and λ is the wavelength of the incident or emitted radiation in microns, for $\varepsilon_{n\lambda}$ denoting the spectral normal emissivity (spectral normal referring to the wavelength dependent measurement of emissivity, measured at the normal to the surface).

Beyond the analysis above, del Campo *et al.* [22] describe general trends in the variation of surface emissivity with wavelength and temperature (consequently, as wavelength of radiation and temperature are related). It is stated that the emissivity decreases with an increasing wavelength, as shown in Fig. 10, and increases slightly with

temperature. The reasons for such a variation involve changing parameters of surface chemistry (such as oxidation), surface activation, phase changes and other probable mechanical changes in surface properties with temperature and wavelength. The heating or cooling of the surface by the incident or emitted radiation at specific wavelengths changes the surface properties, and consequently affects the emissivity as well. The same can be said for the activation energy for certain surface oxidation or reduction processes being provided by the incident radiation at certain wavelengths. All of these factors influence the surface characteristics of the material, leading to changes in the emissivity.

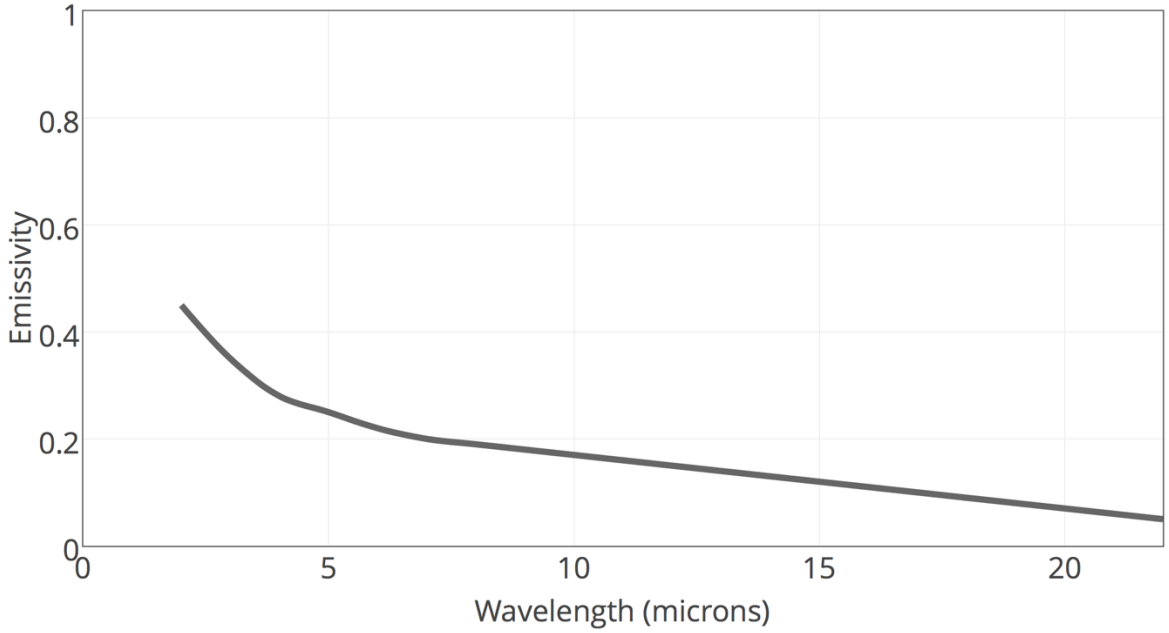

Figure 10. Variation of surface emissivity with wavelength for a sample of brushed Inconel 718, based on observations by del Campo *et al.* [22].

Surface emissivity also varies with the inherent properties of the material of the surface. While metals exhibit very low values (<0.4) for surface emissivity, non-metals and most alloys typically are on the higher end (>0.5) [23]. This is illustrated in Fig. 11, which shows the values for surface emissivity varying with temperature for tungsten (a metal),

silicon carbide (a non-metal) and heavily oxidized stainless steel (an alloy). While the emissivity of tungsten barely reaches 0.3 at its highest, the emissivity of silicon carbide and that of stainless steel is above 0.6 at all points [24].

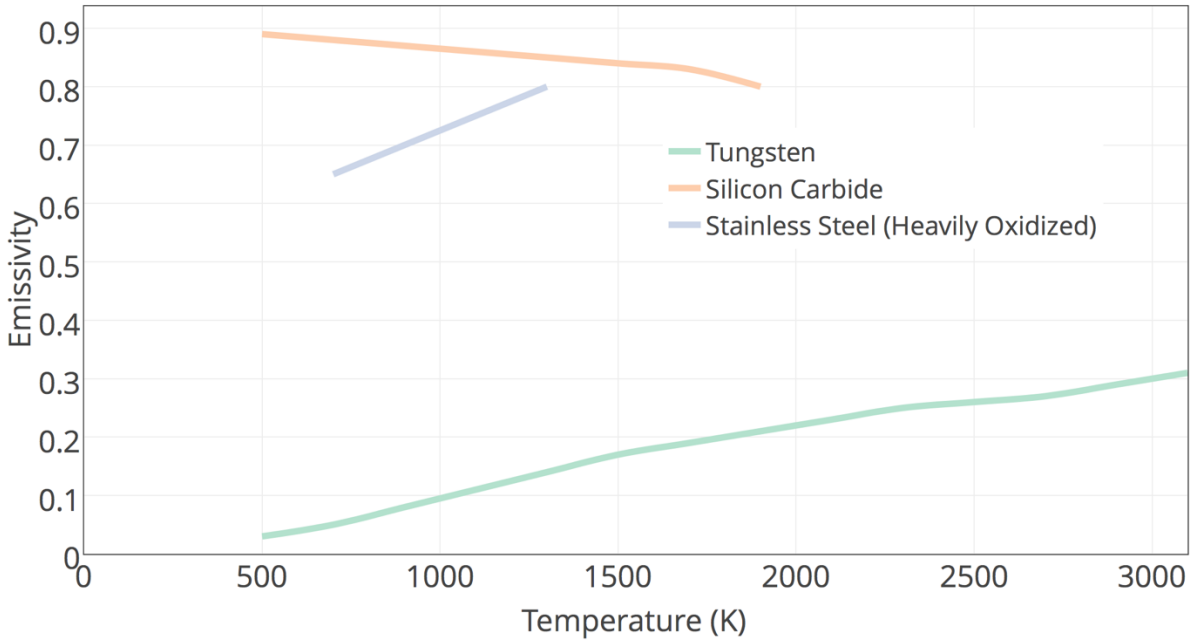

Figure 11. Surface emissivity of tungsten, silicon carbide and heavily oxidized stainless steel, varying with temperature, serving to illustrate the difference in emissivity ranges for metals and non-metals/alloys [23][24].

The variation of surface emissivity with angle of incidence/emission of radiation is quite interesting. Once again, we notice a distinction between metals and non-metals, with metallic surfaces showing an increasing trend for surface emissivity with angle of emission, and non-metallic surfaces showing a variable trend depending on the material under consideration. Both metallic and non-metallic surface emissivity values, however, drop to 0 as the angle approaches 90 degrees [22]. This can be attributed to the fact that at a 90 degree angle of incidence/emission, the incident/emitted photon shows very little/no

interaction with the surface. The general trend for a variation of surface emissivity with angle of emission is depicted in Fig. 12, based on the observations of del Campo *et al.* [22].

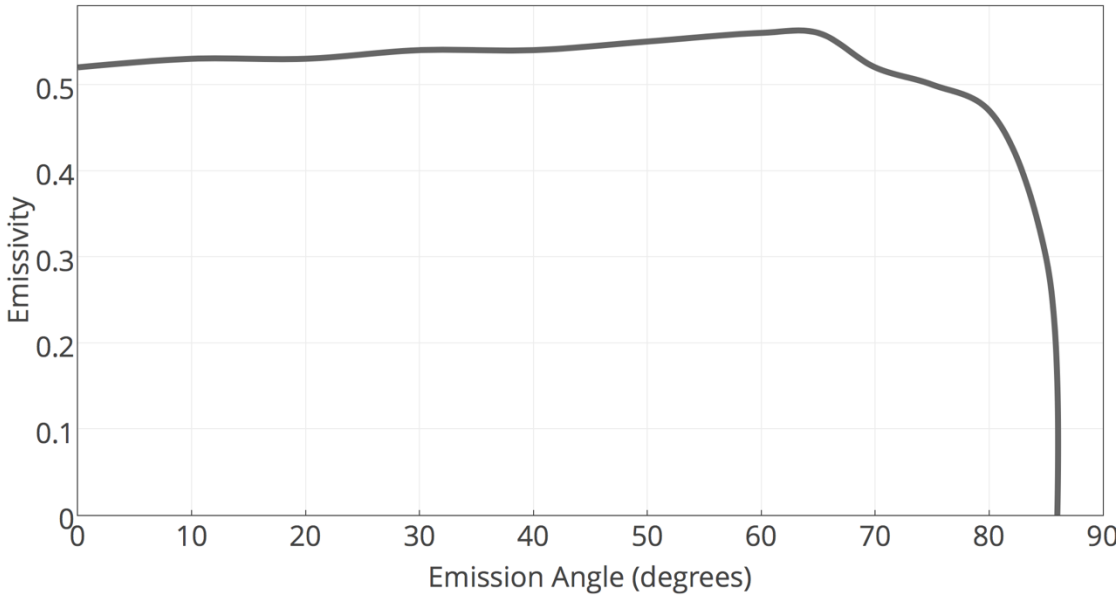

Figure 12. Variation of emissivity with emission angle for a sample of Inconel 718 alloy (incident wavelength of 2.5 microns), showing an almost invariant emissivity value up to an emission angle of 70 degrees, followed by a steep drop to 0 at around 85 degrees [22].

The angle-dependent behavior of surface emissivity can be explained with the help of the modified Ziman theory for surface asperity/specularity [25]. The theory predicts the asperity of a surface, or its ability to scatter light diffusely or in a specular manner, as a function of the surface roughness, the wavelength of radiation, and the emission/incidence angle, as given in Eq. (7), where p is the surface specularity/asperity, σ is the surface roughness, λ is the wavelength of radiation, and θ is the angle.

$$p = \exp\left(-16\pi^3 \frac{\sigma^2}{\lambda^2} (\cos\theta)^2\right) \qquad (7)$$

A plot of the variation of specularity with angle of incidence/emission for various values of the ratio of surface roughness over wavelength is depicted in Fig. 13, showing a steep rise in specularity to a value of 1 as the angle approaches 72 degrees. While this does

not correlate with the drop in emissivity shown in Fig. 12 at an angle of around 85 degrees, it does provide an explanation for the trend in the behavior. A steep rise in the specularity at high angles of incidence indicates a drop in the interaction of the photon with the surface, particularly due the angle of incidence/emission being high. This in turn leads to a steep drop in the emissivity of the surface.

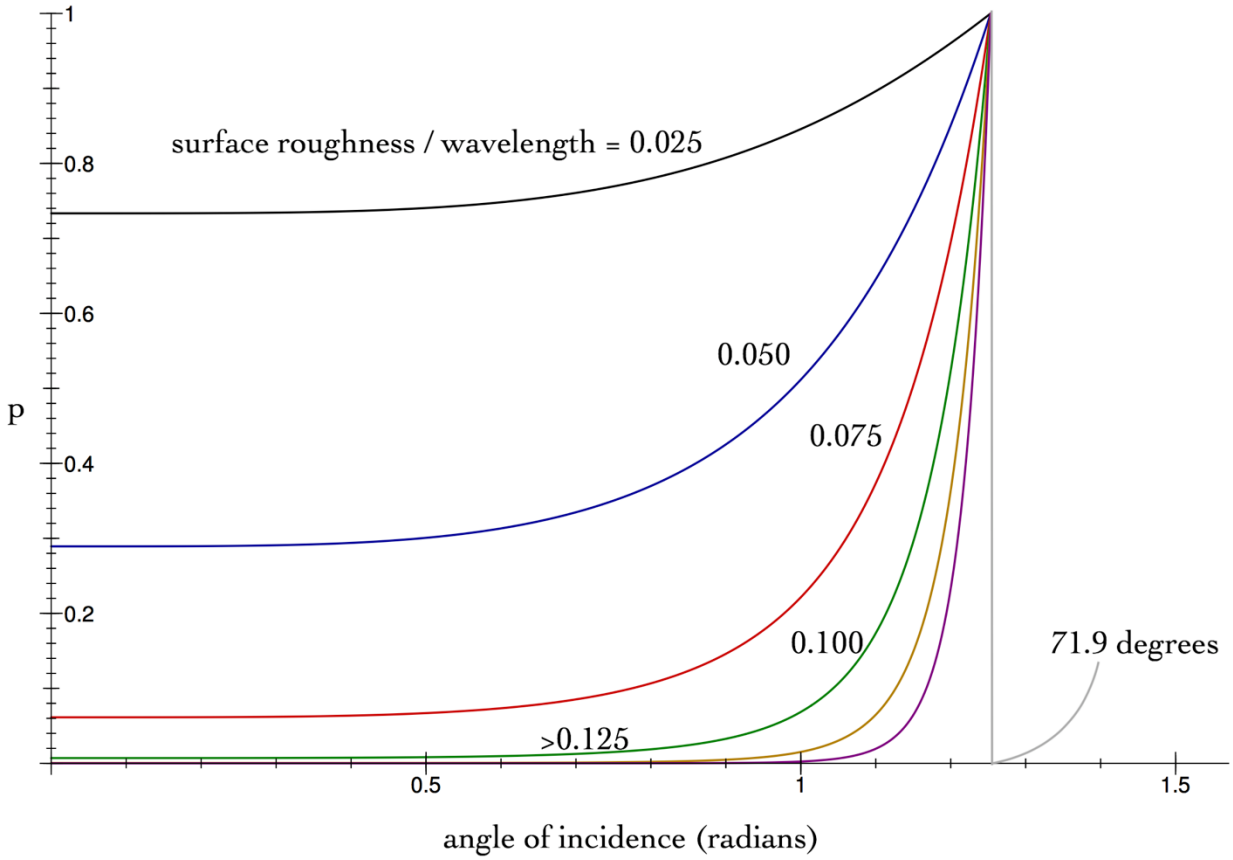

Figure 13. Surface specularity as a function of angle of incidence, as predicted by the modified Ziman theory [25].

As a continuation of the analysis of surface emissivity based on the Ziman theory, another factor that the emissivity depends upon is the surface roughness and the asperity/specularity of the surface. The structural optics of a material are influenced by the surface geometries, which can be represented analytically as surface roughness features. As

detailed in Chapter 2, optical phenomena such as interference and diffraction that occur as a consequence of varying surface roughness features vary the surface emissivity as well. The emissivity also varies with the specularity of the surface, as will be detailed in Chapter 4. The surface specularity and surface roughness are related by the modified Ziman theory, as in Eq. (7), and can be illustrated as in Fig. 14. The variation of the specularity as shown in the figure, and thus the ratio of the surface roughness over the wavelength, directly affects the emissivity as well.

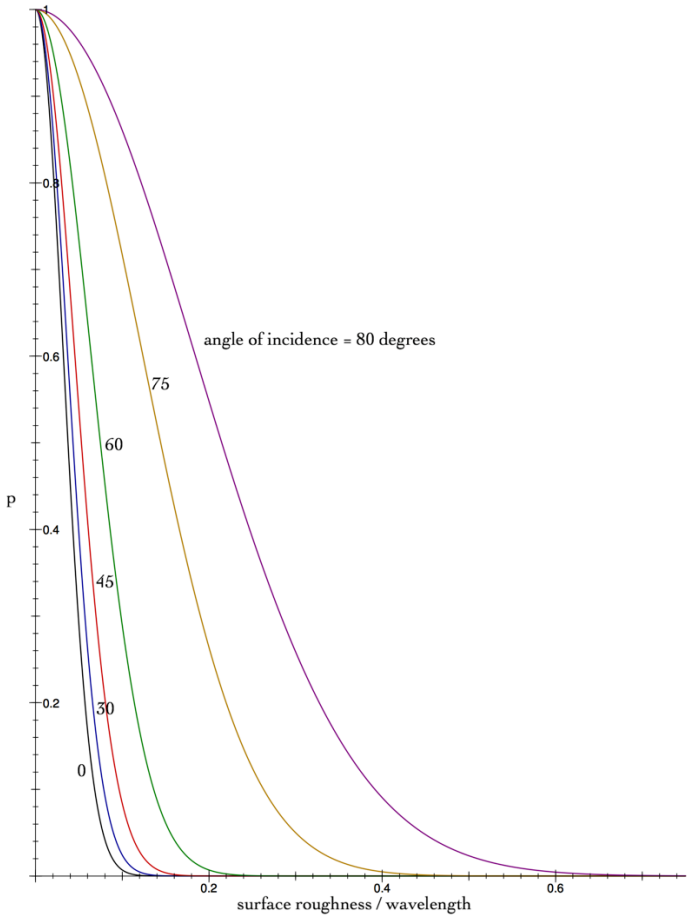

Figure 14. Relationship between surface specularity/asperity and the ratio of surface roughness over wavelength for varying angles of incidence/emission [25].

Computation of the emissivity as a function of the resultant surface roughness is in Chapter 4, with a detailed mathematical and physical analysis for the various regimes of surface specularity.

3.2 Measurement of Surface Emissivity

Measurement or computation of the surface emissivity can either be done experimentally or via modeling and simulation. Experimental measurements of surface emissivity give a more practical result. Various means of measuring surface emissivity for varying surface geometries, angular conditions and spectral conditions have been proposed and demonstrated, including the use of radiometers [22. Direct measurements of emissivity are made calorimetrically or via radiometry [26]. Calorimetric emissivity measurement techniques involve measuring the rate of radiant heat transfer from a sample, which is then compared to that of a blackbody radiator under the same measurement conditions to yield emissivity [27][28]. The rate of radiant heat transfer of the sample is measured in terms of the heat lost by the sample. Direct radiometric emissivity measurement, similar to calorimetric measurement, is made by measuring the radiance of a heated specimen and of a blackbody at the same temperature as that of the sample under the same spectral and geometric conditions [29][30]. The ratio of the two radiances yields the emissivity.

Highly accurate, easily-constructible radiometers in conjunction with Fourier transform infrared (FTIR) spectrometers have been demonstrated to yield the emissivity values for surfaces at various temperatures, angles of measurement and wavelengths by del Campo et al. [22]. Radiometric surface emissivity measurement has also been

demonstrated by Furukawa and Iuchi [26], where radiometers measure the radiance values of a given sample and an idealized blackbody to compute the emissivity of the sample at high temperatures. A similar pyrometric technique has been demonstrated by Herve, Cedelle and Negreanu [31] for simultaneous measurement of surface emissivity and temperature, proposing the use of infrared radiation for the measurements. This method is capable of determining the surface temperature of a material without prior knowledge of the emissivity of the surface, because both the values are determined simultaneously.

The emissivity can also be determined computationally for a given surface using modeling or simulation, as will be discussed in Chapter 4.

CHAPTER 4: COMPUTATIONAL ANALYSIS OF EMISSIVITY

The analysis presented describes the calculation of surface emissivity by modeling or simulation. Sai and Kanamori [32] have used the application of rigorous coupled wave analysis (RCWA) algorithm to simulate optical properties of periodic microstructures, involving a rigorous solution of Maxwell's equations. Chen et al. [33] have shown the use of integral equation method (IEM) to compute the surface emissivity, validated by the use of Monte Carlo simulations of Gaussian surfaces. While the RCWA algorithm is much more computationally expensive than the IEM and Monte Carlo simulations, the latter methods have the drawback of being confined to a few specific demonstrated surface geometries. The IEM methods presently have the capability to compute the emissivity values for surfaces with simple, Gaussian geometries, and as yet do not involve complex geometries, or periodic structures, such as nanowires and multilayers. To mitigate the disadvantages present, the proposal is to use a surface roughness-based computation of the emissivity, eliminating the mathematically rigorous approach of RCWA, while accommodating flexible surface topographies as well.

4.1 Surface Roughness Modeling

Modeling of the surface emissivity of the sample surface is done based on the computation means proposed by Wen and Mudawar [34]. The underlying assumption of the mathematical approach is that the surface emissivity depends on the surface roughness of the sample. In this aspect, the sample can be categorized into various regions, based on the roughness of the surface relative to the wavelength of light incident on it. Neglecting a

perfectly polished (optically smooth) surface (which is the ideal condition), the computations analyze more realistic scenarios of optically rough surfaces. The surface can now be characterized based on the root mean squared (RMS) surface roughness σ, relative to the incident wavelength λ, into the specular region, the intermediate region, or the geometric region. The RMS value of the surface roughness is calculated from the height of the periodic structures from the base of the sample surface, as in Eq. (8).

$$\sigma = \left[\frac{1}{A}\int_A (z - z_m)^2 \cdot dA\right]^{1/2} \qquad (8)$$

A is the area measured, while (z-z_m) gives the deviation of the structure from the mean surface. In the specular region, the ratio σ/λ is less than 0.2, while the intermediate region has $0.2 < \sigma/\lambda < 1$, and the geometric region accommodates values above the intermediate region, with $\sigma/\lambda > 1$.

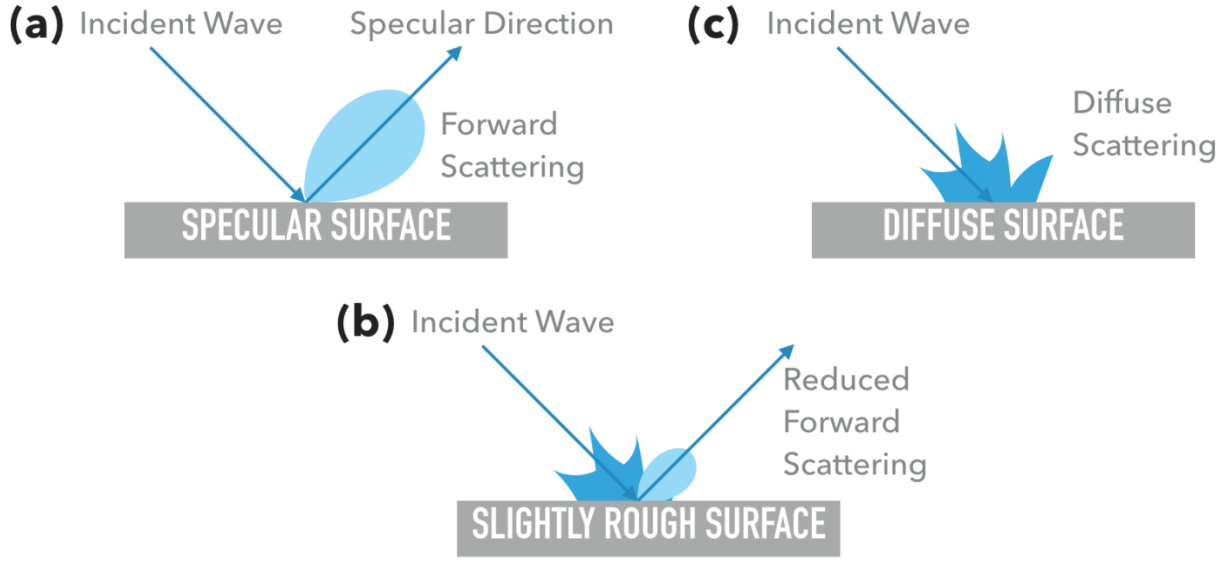

Figure 15. Details of the distinction between the three regimes of surface roughness: (a) shows a specular surface, (b) shows one in the intermediate region, and (c) shows a diffuse surface.

As shown in Fig. 15, the specular region is so named as it reflects any incident radiation in a specular manner, where the angle of incidence and the angle of reflection are equal. In the geometric region, the angle of reflection does not necessarily equal the angle of incidence, and can range over any value from 0 to 180 degrees.

4.2 Regimes of Surface Roughness

For those incident wavelengths and/or surface roughness where the ratio of σ/λ is less than 0.2, the surface is assumed to be optically specular, entailing that the angle of incidence equals the angle of reflection. DeWitt *et al*. [35] compute the emissivity of the surface (based on the reflectance), using diffraction theory, assuming the surface heights to have a Gaussian distribution.

$$\rho_{\mathrm{r}} = \rho_{\mathrm{p}} \exp\left[-\left(\frac{4\pi\sigma}{\lambda}\right)^2\right] \tag{9}$$

$$\rho_{\mathrm{p}} = \frac{4n^2}{(n+1)^2+\kappa^2} \tag{10}$$

$$\kappa = \frac{\alpha\cdot\lambda}{4\pi} \tag{11}$$

ρ_{r} gives the reflectance of the rough surface we aim to compute, and ρ_{p} is the reflectance of the polished sample surface, for which data is readily available, or can be computed as a function of the refractive index (n) and extinction coefficient (κ) of the sample, as shown in Eq. (10). The value of the extinction coefficient depends upon the absorptivity (α) of the sample, evidenced by Eq. (11).

In the intermediate region, Wen and Mudawar [34] propose the use of the bidirectional reflectance function (BDRF) to quantify the emissivity of the surface as a function of its surface roughness. The function involves the use of incident and scattered

components for the angle of energy, radiant power flow, and the solid angle. The BDRF equation is given as a function of these parameters in Eq. (12). We then use electromagnetic scattering theory to estimate the spectral reflectance in Eq. (13), and consequently, the emissivity using Kirchhoff's law as in Eq. (14).

$$\rho''_{\lambda}(\theta_i, \theta_s) = \frac{\frac{\pi}{\cos\theta}\cdot\frac{d\Phi_s}{d\Omega_s}}{\frac{d\Phi_i}{d\Omega_i}} \tag{12}$$

$$\rho'_{\lambda}(\theta_i) = \frac{1}{\pi}\int_{2\pi}\rho''_{\lambda}(\theta_i, \theta_s)\cos\theta_s d\Omega_s \tag{13}$$

$$\varepsilon'_{\lambda}(\theta_i) = 1 - \rho'_{\lambda}(\theta_i) \tag{14}$$

Here, θ_i and θ_s refer to the incident angle and scattered angle, while Ω_i and Ω_s refer to the incident and scattered solid angle, and Φ to the radiant power flow. We then use Kirchhoff's approximation to evaluate a numerical solution for the emissivity as a function of the surface roughness [34]. This avoids the shortcomings of the Fresnel and Lambertian approximations, which assume, respectively, a specular and diffuse approximation for the phenomena, and fail to account for surface geometries or other parameters and the effects of the incident wavelength.

The geometric region is primarily affected by the surface geometry of the sample. The effects of the surface roughness on the computed emissivity values begin to outweigh the optical effects contributed by the wavelength of incident light, and a detailed evaluation of the surface geometry/topography is necessary. The surface emissivity is then evaluated as a function of the surface topography. Modest [36] presents a means of evaluating the surface emissivity as a function of surface topography for periodic structures on the surface. Assuming the surface roughness features on the sample to be periodic in nature, it is possible to apply this method to evaluate the emissivity of the surface, as a function of

the periodicity of the structures, and their physical dimensions, and other parameters, as shown in Eq. (15).

$$\varepsilon_{\mathrm{r}}(\theta) = \int_{-\infty}^{+\infty} [1 - \rho_{\mathrm{p}}(\theta - \tan^{-1} p)] \, |1 - p \cdot \tan\theta| P(p) \cdot dp \qquad (15)$$

$$\rho_{\mathrm{p}} = \frac{(n-1)^2 + \kappa^2}{(n+1)^2 + \kappa^2} \qquad (16)$$

$$P(p) = \frac{\sigma_l}{2\sqrt{\pi}\sigma_h} \exp\left[-\left(\frac{p\sigma_l}{2\sigma_h}\right)^2\right] \qquad (17)$$

ε_{r} gives the emissivity of the rough surface, with ρ_{p} being the reflectance of an optically smooth sample of the material, computed as a function of the refractive index and extinction coefficient, as in Eq. (16). Eq. (15) gives the value of the emissivity as dependent on *p*, which is the tangent of the difference between the angle of the incident field and the angle of incidence of the photons. *P(p)*, then, in Eq. (17), gives the probability of an event occurring at a given value of *p*. The spacing between two adjacent structures in the periodic arrangement is given by σ_l, while σ_h is the RMS value of the surface roughness, calculated from the height of the periodic structures from the base of the sample surface, as in Eq. (8).

The periodic structures measured as functions of the surface roughness depend on the area measured, the average deviation of the structure from the mean surface, the dimensions of the structures themselves (width, length and height), and the periodicity. A consequence of using the RMS surface roughness for the calculation of the emissivity dependence and values is the possibility of a variety of surface geometries and topographies. We discuss here the evaluation of different possible bio-inspired surface topographies, with a basis in the coloration of the wings of the *Morpho* butterfly.

4.3 Validation of Surface Roughness Model

The validity of the surface roughness model described above, and of the use of the nanowire trees as a valid representation of the structures on the wings of a *Morpho* butterfly is done by comparison of the emissivity spectrum of the modeled Christmas-tree structures with existing literature. Potyrailo *et al*. [20] demonstrate a modified Christmas-tree architecture based on the *Morpho* butterfly for vapor sensing applications, while Steindorfer *et al*. [37] demonstrate a simulation of the butterfly wing nanostructures and their spectrum. The emissivity spectrum of the proposed Christmas-tree architecture, with dimensions as detailed by Siddique et al. [16] is then compared with data from Potyrailo *et al*. [20] and Steindorfer *et al*. [37]. The surface topography considered for modeling is a periodic "Christmas-tree" structure, closely resembling the butterfly wing structures, with central ridges that support branches of lamellae on either side. The Christmas-tree is of similar dimensions as the wing structures, with ridge heights of 1.25 microns, ridge spacing of 1.25 microns, and lamellae spacing of nearly 200 nm. The lamella length ranges from around 29 nm at the tips of the Christmas-trees, increasing by roughly 40-45 nm with each adjacent lamella on the alternate side of the ridge. The lamellae reach a maximum length of around 318 nm, up until the base of the structure, as illustrated in Fig. 16. The emissivity spectrum of this topography closely matches data in existing literature [20][37], and is shown in Fig. 17.

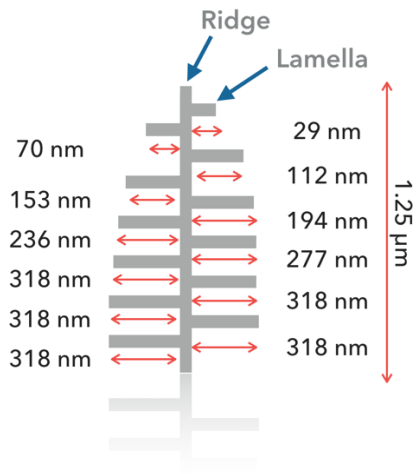

Figure 16. Dimensions of the Christmas-tree structures used for computation, with data based on Siddique *et al*. [16], showing a gradually increasing lamella length down the length of the ridge, with a ridge height of 1.25 microns, and a lamella spacing of 200 nm.

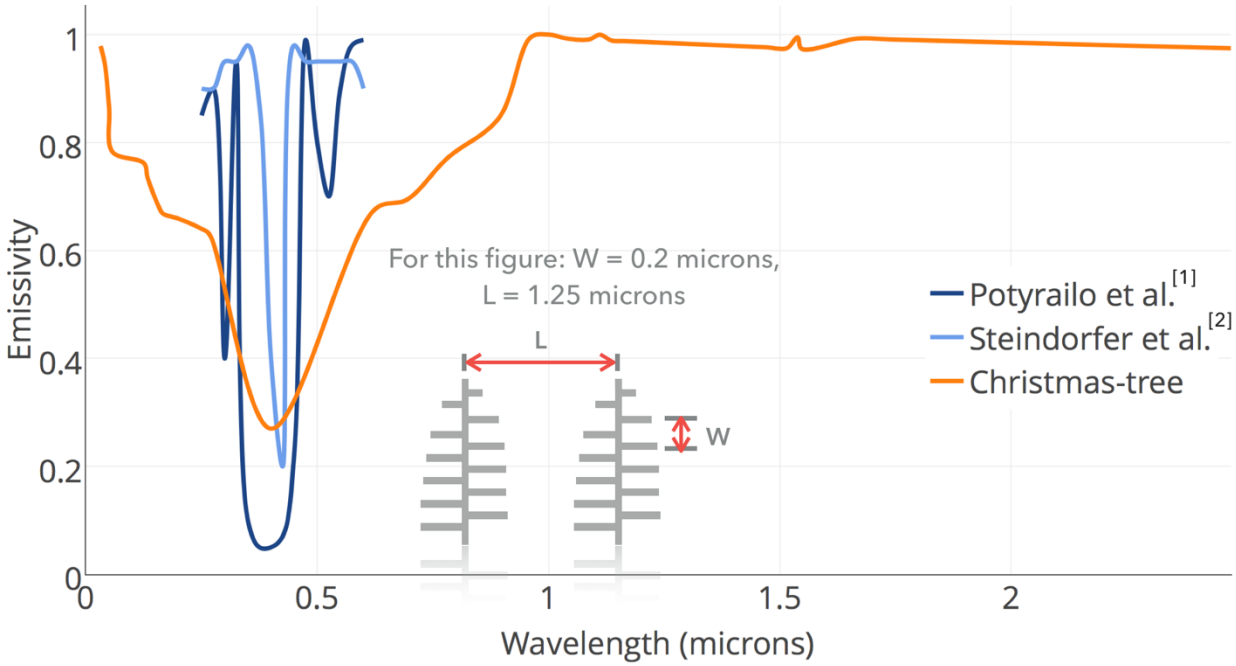

[1] Potyrailo et al. - Nature Communications (2015)
[2] Steindorfer et al. - Optics Express (2012)

Figure 17. Emissivity spectrum for the Christmas-tree structures computed using this study, with a ridge spacing of 1.25 microns and a lamella spacing of 200 nm, showing a dip in the blue region of the spectrum. Comparison done with data from Potyrailo *et al*. [20], and Steindorfer *et al*. [37], showing an emissivity dip in similar wavelengths of the spectrum.

The emissivity spectrum for the Christmas-tree nanostructures shows a fairly high value (>0.8) upto nearly 100 nm, beyond which it gradually dips. The emissivity then regains its high value (>0.8) beyond a wavelength of around 800 nm). This dip in emissivity is centered around 418 nm (centered around a dip dropping from 116 nm rising up to 722 nm), which compares well with the dips of Potyrailo *et al*. [20], centered around nearly 400 nm, and Steindorfer *et al*. [37], centered around nearly 450 nm. The emissivity dip, and consequent reflectivity peak for the proposed Christmas-tree structures lay in the blue region of the visible spectrum, and corresponds with the blue coloration of the wings of the *Morpho* butterfly. These results are also echoed in the findings of Huang, Wang and Wang [38], with regards to the reflectivity peak at the blue region of the spectrum, thus validating the use of the surface roughness model for emissivity computation, and the application of the Christmas-tree structures as a simulation of the structures on the wings of the *Morpho* butterfly. The Christmas-tree structure is, therefore, taken to be a close biomimetic model of the butterfly wing nanostructures.

4.4 Model Set-Up/Parameters

The validation of the Christmas-tree structures as a comparable model to the *Morpho* butterfly nanostructures leads to the development of a tailored Christmas-tree nanostructure with a selective high emissivity over the atmospheric transmission window. The requirement for a high emissivity between the wavelengths of 8 and 14 microns yields the ridge spacing as 13.86 microns and the lamella spacing as 24.25 microns. The lengths of the lamellae reach a maximum at the base of the ridge, being around 3.46 microns long. The

lamellae at the tips of the ridges are roughly 70 nm long, with an increment in length of around 80 nm between each lamella down the ridge, up to a maximum lamella length of around 310 nm. The design for the lamellae length roughly follows the design proposed by Siddique *et al*. [16].

The choice of the material used for the nanostructures depends on the intended application. The use of silica (SiO_2) in solar cells has been demonstrated, most prominently by Zhu *et al*. [10], and Raman *et al*. [11], primarily due to the transparent nature of silica and its high transmissivity in the visible region of the solar spectrum. Another possible material is alumina (Al_2O_3), due to its widespread utilization and ease of use as a manufacturing material. The use of alumina in the aircraft and aerospace industry has also been widely demonstrated [39][40]. The use of alumina is also bolstered by the closeness of the refractive indices of alumina and silica for the range of wavelengths that are being evaluated [41-43] as shown in Fig. 18(a), with the wavelength-dependence of the refractive indices being evaluated with the help of data from Stephenson [44].

Alumina also displays a high level of transmissivity (>80%) for a majority of the spectrum [45][46], as shown in Fig. 18(b), solidifying its application for thermal management and for related solar applications.

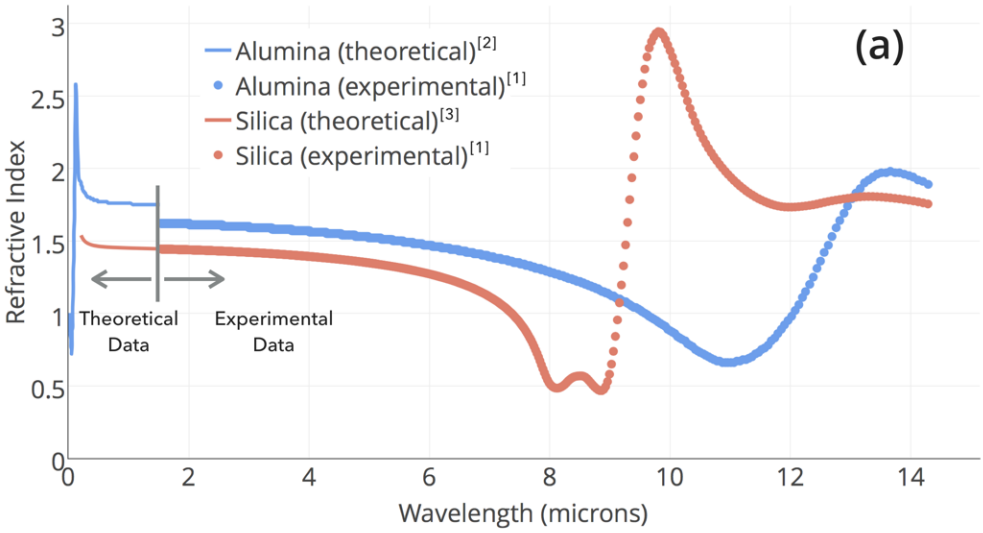

[1] Kischkat et al. - Appl. Opt. (2012) (data above 1.54 microns)
[2] Malitson and Dodge - J. Opt. Soc. Am. (1972) (data below 1.54 microns)
[3] Malitson - J. Opt. Soc. Am. (1965) (data below 1.54 microns)

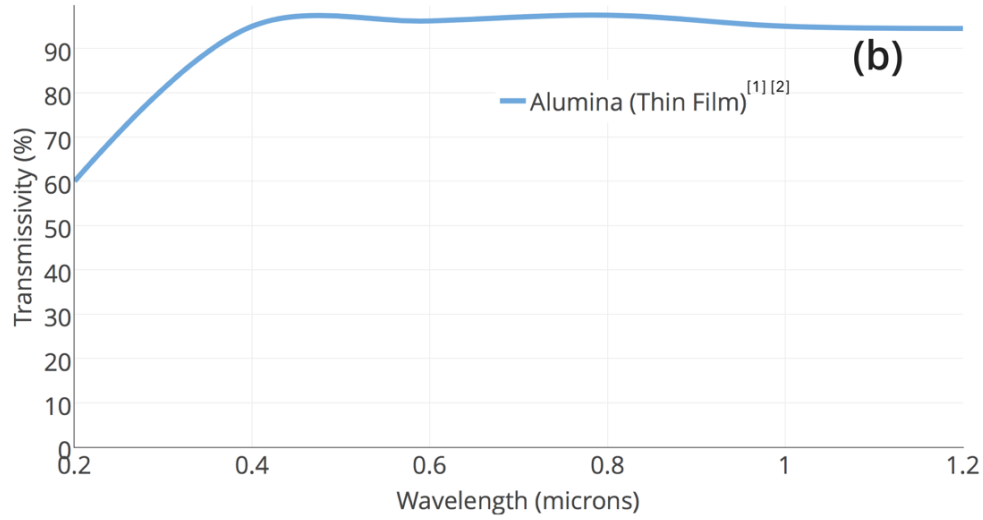

[1] Vitanov et al. - Jpn. J. Appl. Phys. (2006)
[2] Choi et al. - Current Applied Physics (2012)

Figure 18. Optical characteristics of materials used for the manufacturing of photonic structures. (a) Comparison of the refractive indices of alumina and silica, with data from Malitson and Dodge [41], Kischkat [42] and Malitson [43], showing average refractive indices for both materials to be very comparably close to each other. Deviations and variations in the refractive index values are due to atomic interactions and lattice structure. (b) Transmissivity profile of alumina, with data from Vitanov et al. [45] and Choi et al. [46], showing high transmissivity values, validating its use for solar applications.

4.5 Computation Results

The emissivity spectrum for this structure is given in Fig. 19, where it is compared with the emissivity spectra for bare alumina [41][42] and bare aluminum [47]. The purpose of the Christmas-tree nanostructure is validated when compared to bare alumina and/or aluminum, as these both yield a relatively flat emissivity over the entire spectrum. This would not serve the purpose of a surface with a tunable emissivity. The emissivity spectrum of these Christmas-tree structures follows the peak in the atmospheric transmission window, rising roughly at 8 microns, and dropping off at around 14 microns. The emissivity through the rest of the spectrum is low, maintaining a value of around 0.1 for most of the visible region. This leads to a high reflectivity for the surface over all wavelengths, except for those between 8 and 14 microns, effectively aiding the reemission of radiation over the infrared window, while avoiding heat generation by reflecting incident radiation over other wavelengths. The emissivity spectrum of the Christmas-tree structures also roughly follows the trend of the multilayer photonic cooler of Raman *et al*. [11], showing a better performance at farther regions of the thermal wavelengths, with a higher reflectivity. A close emulation of the nanostructures on the wing of the *Morpho* butterfly has been demonstrated by Butt et al. [19] using atomic layer deposition (ALD), where precursors react with one another to form a layer of the desired material that is of atomic thickness [48][49].

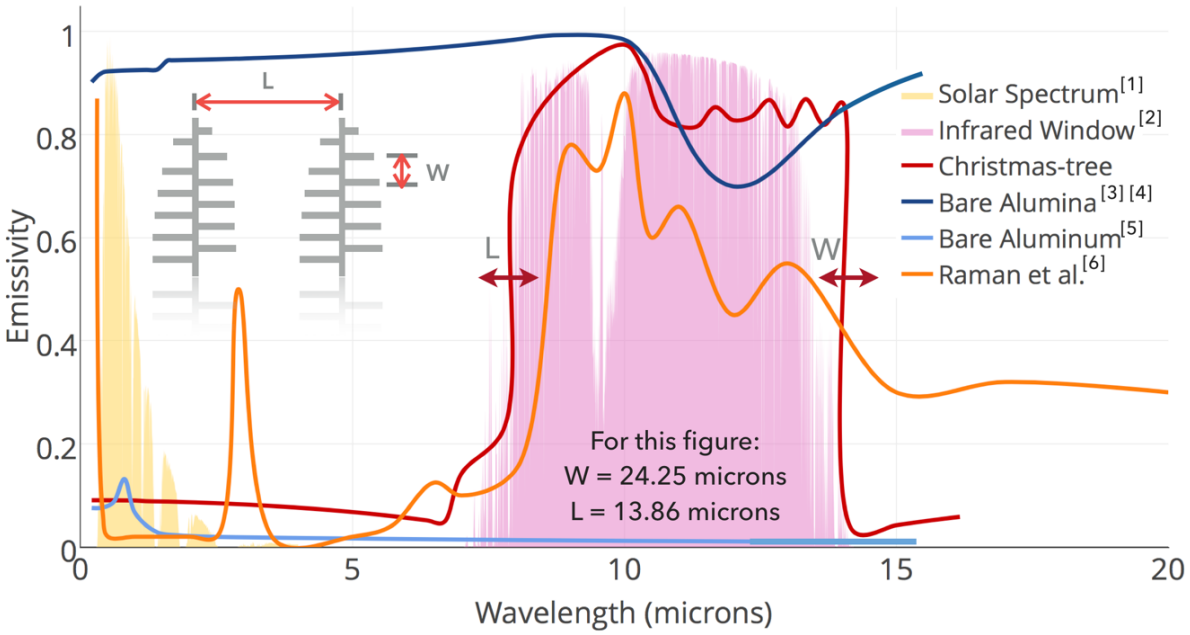

[1] ASTM G173-03, American Society for Testing and Materials (2012)
[2] Lord, S.D. - NASA Technical Memo. 103957 (1992)
[3] Kischkat et al. - Appl. Opt. (2012)
[4] Malitson and Dodge - J. Opt. Soc. Am. (1972)
[5] Rakić et al. - Appl. Opt. (1998)
[6] Raman et al. - Nature (2014)

Figure 19. Emissivity spectrum for the Christmas-tree nanostructure, with a ridge spacing (L) of 13.86 microns and a lamella spacing (W) of 24.25 microns, compared with the emissivity spectra of bare alumina [41][42] and bare aluminum [47]. The spectra are superposed on the solar spectrum in the visible region [1] and the atmospheric transmission window [2]. Christmas-tree spectrum is compared with multilayer photonic cooler proposed by Raman *et al*. [11].

The adaptability of the Christmas-tree nanostructures used for thermal management to various emissivity requirements is aided by flexibility in varying the dimensions of the ridge spacing and the lamella spacing. The rise in the high emissivity region is controlled by the ridge spacing, as a result of the interference of photons over multiple adjacent ridges. Increasing the ridge spacing leads to a delayed rise in the high emissivity region, and a decrease in the ridge spacing yields an earlier rise in the high emissivity region, as shown in Fig. 20(a). Similarly, the drop in emissivity at the end of the high emissivity region is controlled by the lamella spacing, shown in Fig. 20(b). Varying the

periodicity of the lamellae varies the wavelength response due the interference of photons between adjacent lamellae. Increasing the lamella spacing delays the drop in emissivity, as does bringing the lamellae closer cause an earlier drop in emissivity. The tunable nature of the photonic structures is similarly reported by Huang, Wang and Wang [38], with variations in the periodicity of the structures yielding varying reflectance peaks.

The results show a tunable periodic nanostructure that effectively reemits incident radiation from the surface through the atmospheric transmission window. The high emissivity regions correspond to the thermal regions of the wavelength, thus avoiding the detrimental effects of undesirable heat generation on the surface. The surface also exhibits a high reflectivity for all other regions of the spectrum, thus effectively avoiding the heating of the surface by any incident radiation on it. The adaptability of the structure to various requirements posed on it is aided by the flexibility in its design and dimensions, with varying periodicities in different aspects of the structure resulting in the tuning of emissivity in different regions of the spectrum.

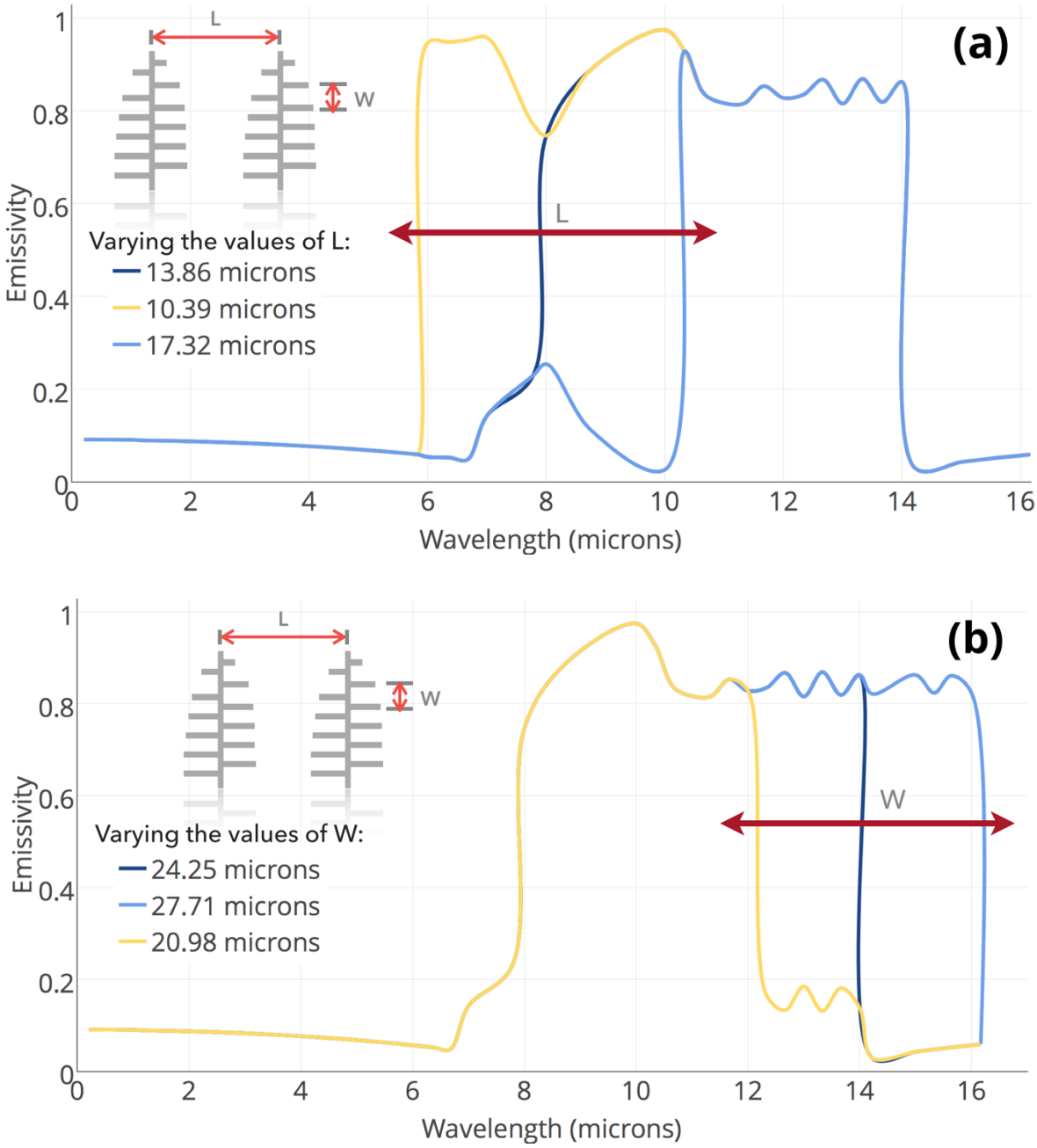

Figure 20. Tunable nature of the Christmas-tree structures aided by the variation of the ridge and lamella spacing. (a) Variation in periodicity of ridges leading to either a delayed rise in high emissivity or an early rise. (b) Variation in lamellae periodicity similarly yielding a delayed drop in high emissivity or an early rise. Variations in dimensions are chosen to depict a rise at either 6, 8 or 10 microns, and a drop at either 12, 14 or 16 microns.

Use of the Christmas-tree structures for solar applications demands a low reflectivity, or high absorptivity/emissivity for the visible region of the solar spectrum (between 200 nm and 1100 nm). The resultant modification in the dimensions of the Christmas-tree structures required to fit this new profile yields a ridge spacing of 13.86 microns, with a lamella spacing of 1.91 microns. The lengths of the lamellae follow the same pattern as proposed before, for the results in Fig. 19. The emissivity spectrum for the modified Christmas-tree structures is illustrated in Fig. 21. The emissivity profile is compared with that of bare alumina [41][42] and bare aluminum [47]. The data is also compared with that of the photonic cooler proposed by Zhu *et al*. [10], which proposes a radiative cooling solution for solar absorbers.

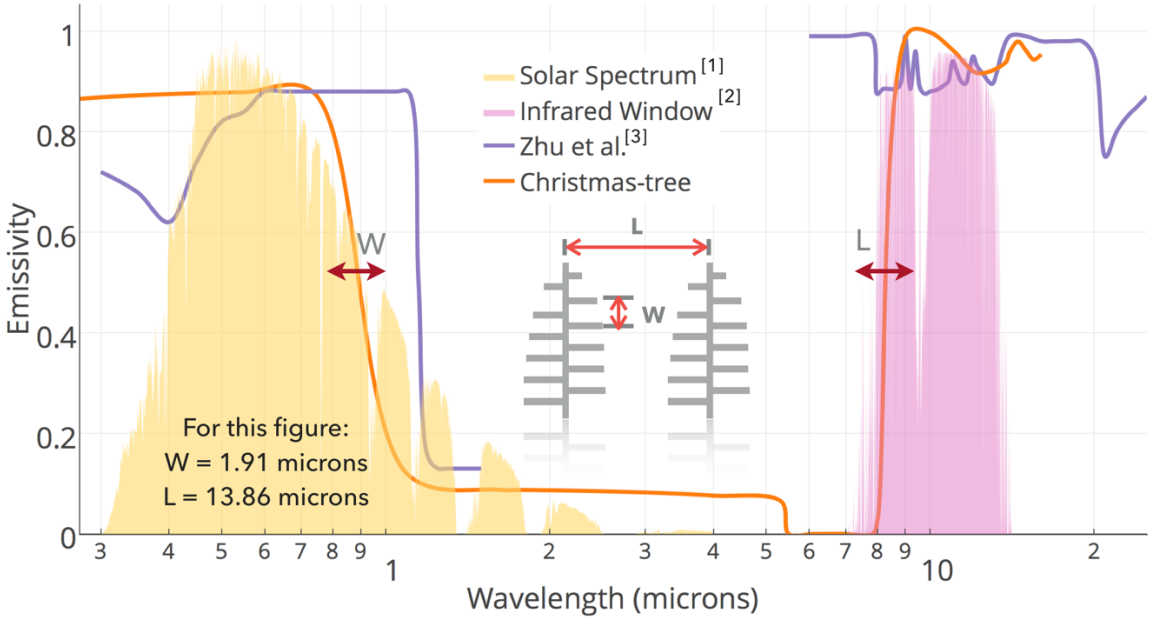

Figure 21. Emissivity spectrum for the modified Christmas-tree nanostructure, with a ridge spacing (L) of 13.86 microns and a lamella spacing (W) of 1.91 microns, compared with the emissivity spectra of bare alumina [41][42] and bare aluminum [47], superposed on the solar spectrum in the visible region [1] and the atmospheric transmission window [2]. The data is further compared with the emissivity spectrum of the solar absorber photonic structure proposed by Zhu *et al*. [10].

The Christmas-tree structures now demonstrate an elevated emissivity/absorptivity value (>0.8) between the wavelengths of 200 and 1100 nm, dropping off to below 0.1 beyond it. This precedes a rise in emissivity to greater than 0.8 beyond 8 microns. This aids in the effective absorption of the visible regions of the solar spectrum, facilitating the functioning of the solar device. The emissivity spectrum also roughly follows that of the solar absorber photonic structures of Zhu *et al*. [10], though the emissivity values demonstrated by Zhu *et al*. peak beyond 6 microns itself, instead of the 8 microns demonstrated by the Christmas-tree structures, leading to unnecessary absorption of wavelengths not within the atmospheric transmission window. This has the potential to lead to undesirable heat generation due to the absorption of radiation in the thermal wavelengths, and is minimized by the modified Christmas-tree structures.

CHAPTER 5: THERMAL ANALYSIS

5.1 Thermal Radiation Model

Analysis of the effectiveness of the Christmas-tree nanostructures is done by modeling the steady state temperature of the surface. Assuming that the surface is exposed to incident radiation with a clear sky at all times, the power balance on the surface is a combination of the incident solar irradiance (P_{sun}), the incident atmospheric thermal radiation (P_{atm}), the radiation emitted by the surface (P_{rad}) and the conductive and convective losses from the surface ($P_{cond+conv}$), as given by Eq. (11) [10]. The surface temperature is denoted as T, with the ambient temperature at T_{amb}.

$$P_{rad}(T) - P_{atm}(T_{amb}) - P_{sun} + P_{cond+conv} = 0 \quad (11)$$

The radiation emitted out from the surface is computed by multiplying the radiance of a black body with the emissivity of the surface, integrated over the hemisphere, as in Eq. (12).

$$P_{rad}(T) = \int \cos\theta \, d\Omega \int_0^{\infty} I_{BB}(T,\lambda)\varepsilon(\lambda,\Omega)d\lambda \quad (12)$$

$$\int d\Omega = \int_0^{\pi/2} \sin\theta \, d\theta \int_0^{2\pi} d\phi \quad (13)$$

$$I_{BB}(T,\lambda) = \frac{2hc^2}{\lambda^5(e^{hc/\lambda k_B T}-1)} \quad (14)$$

Eq. (13) gives the angular integral over the hemisphere, while Eq. (14) computes the radiance of a blackbody at a temperature T, with λ being the wavelength, h representing the Planck constant, c the velocity of light in vacuum, and k_B the Boltzmann constant.

The incident atmospheric thermal radiation is computed similar to Eq. (12), factoring in the emissivity of the atmosphere (ε_{atm}), with t being the atmospheric transmittance along the zenith.

$$P_{atm}(T_{amb}) = \int \cos\theta \, d\Omega \int_0^\infty I_{BB}(T,\lambda)\varepsilon(\lambda,\Omega)\varepsilon_{atm}(\lambda,\Omega)d\lambda \qquad (15)$$

$$\varepsilon_{atm}(\lambda,\Omega) = 1 - t(\lambda)^{1/\cos\theta} \qquad (16)$$

The incident solar power absorbed by the surface is computed in Eq. (17), where θ_{sun} is the incident angle. The solar irradiance is taken for an air mass of 1.5 (AM1.5) [50].

$$P_{sun} = \int_0^\infty I_{AM1.5}(\lambda)\varepsilon(\lambda,\theta_{sun})\cos\theta_{sun}\, d\lambda \quad (17)$$

Conductive and convective heat losses from the surface are computed in Eq. (18), where h_c is the net heat transfer coefficient for conduction and convection from the surface to its surroundings.

$$P_{cond+conv} = h_c(T - T_{amb}) \qquad (18)$$

The surface is assumed to have a tilt of 30°, with the h_c at 6.9 W/m^{2}K, to provide a comparison with the passive radiative cooler developed by Raman *et al*. [11]. The model also assumes that the sky is clear throughout the day, and that the effects of wind are neglected, so as to maintain a uniform value for the heat transfer coefficient.

5.2 Temporal Temperature Profile

The hourly temperature profile is modeled for daylight hours, as illustrated in Fig. 22. The performance of the Christmas-tree nanostructures is compared with the photonic cooler developed by Raman *et al*. [11], and shows a surface that is cooler by nearly 1-3ºC for the Christmas-tree structures, overall. This data is also compared with the performance of polished, bare alumina, which reaches a peak temperature of around 77ºC, more than

50ºC hotter than ambient temperature. Overall, the Christmas-tree structures maintain a surface temperature that is between 50% and 90% cooler than the polished alumina surface. This is primarily due to the high absorptivity of alumina over the entire incident spectrum, which causes it to heat up.

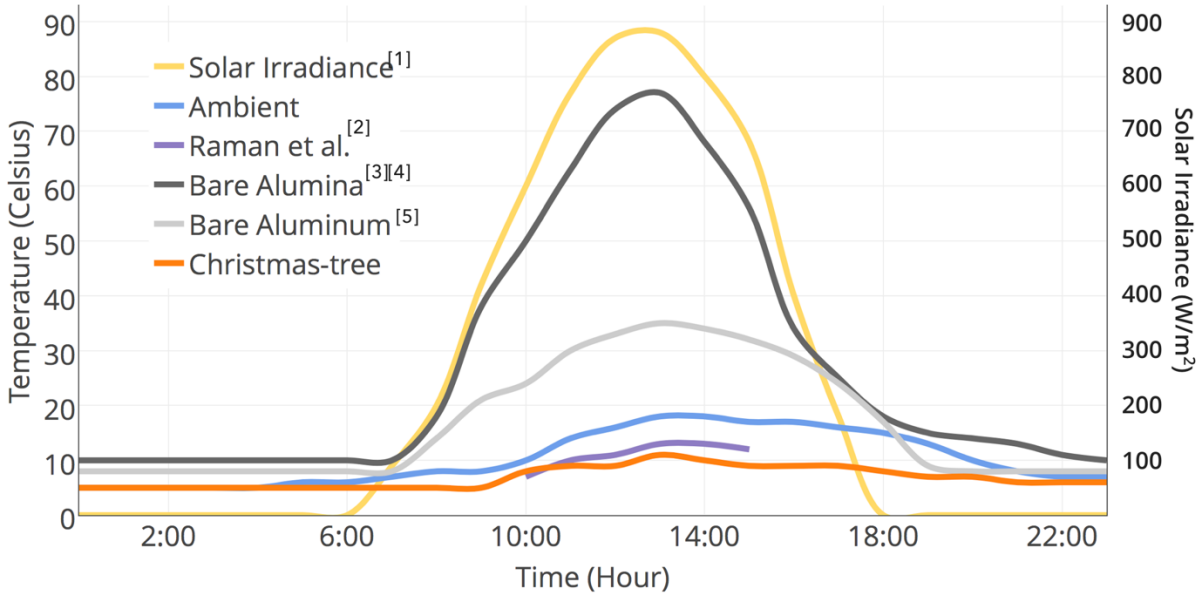

[1] Coddington et al. - Bull. American Meteorological Soc. (2015)
[2] Raman et al. - Nature (2014)
[3] Kischkat et al. - Appl. Opt. (2012)
[4] Malitson and Dodge - J. Opt. Soc. Am. (1972)
[5] Rakić et al. - Appl. Opt. (1998)

Figure 22. Modeling of the performance of the Christmas-tree nanostructures for a clear sky with no wind, superposed on the solar irradiance [50]. Data compared with photonic cooler proposed by Raman *et al*. [11], and with polished bare alumina surface [41][42] and polished bare aluminum [47].

CHAPTER 6: LIMITATIONS AND SCOPE FOR FUTURE WORK

The model presented in this study comes with a set of drawbacks and limitations, key among which is the requirement of further validation of the model by means of numerical analyses, or, ultimately, experimental methods. This is necessary to analyze and mitigate any detrimental effects caused by practical use of materials and surfaces. The model assumes ideal performance of material optical and electronic properties, and does not account for any real-life deviations from the normal. One such drawback is the assumption that surface topographies with similar surface roughness values behave similarly, wherein the intricacies in the material texture are harder to compute with the proposed method. Actual measurements of the properties, such as surface emissivity, might vary from the model presented.

The computational model presented here does not account for the consequences of real-time measurement and the limitations posed on the set-up due to material properties or equipment specifications. Practical applications of the nanowire tree structures for thermal management would also need to take into account the effects of other modes of heat transfer. While the effects of convection can be minimized to a great extent realistically, conduction would still need to be accounted for.

Experimental procedures for the measurement to support the ideal results presented here would lead to a better understanding of the bio-inspired nanostructures.

CHAPTER 7: SUMMARY AND CONCLUSIONS

In this thesis, an introduction to the effects of incident radiation on surfaces was offered, with a need for a resultant surface thermal management. A literature review of the existing solutions to the issues was discussed (Chapter 1), with the drawbacks of the existing solutions posed as the motivation for the present study. A novel bio-inspired solution to surface thermal management by passive radiative cooling was proposed (Chapter 2), and its surface characteristics (emissivity) were computed (Chapters 3, 4). A thermal analysis of the proposed solution was offered (Chapter 5) as a test of its practical viability. The results have thus demonstrated, by simulation of mathematical models, a bio-inspired nanostructure that helps in radiative cooling of surfaces exposed to solar radiation, by exploiting the atmospheric transmission window of the earth's atmosphere. Previous studies [3-11] have demonstrated various solutions for thermal management by nanowires and nanostructures. While active cooling solutions [3-5] come with caveats in finances and power consumption involved, passive cooling solutions from existing studies [6-11] and the present study mitigate the issues. Previous attempts at passive cooling have either resulted in a lack of spectral selectivity for the emissivity control [6], a lower level of accuracy in following the atmospheric transmission window [10][11] leading to unnecessary absorption of thermal wavelengths, use of economically expensive materials, or impractical manufacturing processes. The proposed nanowire trees/Christmas-tree structures also demonstrate an improved cooling performance compared to existing photonic coolers [10][11], maintaining a lower overall surface temperature for incident daylight sunlight. The use of alumina in this model is presented as a cheap manufacturing

material, with a proven practical application in various industries [39][40]. Alumina also presents a wide variety of options in the method of manufacturing. Moreover, the Christmas-tree structures have been shown to be a viable candidate for mass production [51], thus providing for a practical day-to-day solution. These, coupled with the highly tunable nature of the structures, presents a viable alternative to the problem of heat generation on surfaces with incident solar radiation and its solution by radiative cooling.

REFERENCES

[1] Victoria, M., Domínguez, C., Askins, S., Antón, I., & Sala, G. (2012). ASTM G173 standard tables for reference solar spectral irradiances. *Japanese Journal of Applied Physics*, *AM15D*, 10ND06. http://doi.org/10.1143/JJAP.51.10ND06

[2] Lord, S. D. (1992). *Technical Memorandum 103957*. Tech. rep., NASA.

[3] Al-Amri, F., & Mallick, T. K. (2013). Alleviating operating temperature of concentration solar cell by air active cooling and surface radiation. *Applied Thermal Engineering*, *59*(1-2), 348–354. http://doi.org/10.1016/j.applthermaleng.2013.05.045

[4] Najafi, H., & Woodbury, K. A. (2013). Optimization of a cooling system based on Peltier effect for photovoltaic cells. *Solar Energy*, *91*, 152–160. http://doi.org/10.1016/j.solener.2013.01.026

[5] Moharram, K. A., Abd-Elhady, M. S., Kandil, H. A., & El-Sherif, H. (2013). Enhancing the performance of photovoltaic panels by water cooling. *Ain Shams Engineering Journal*, *4*(4), 869–877. http://doi.org/10.1016/j.asej.2013.03.005

[6] Hsu, P. C., Liu, X., Liu, C., Xie, X., Lee, H. R., Welch, A. J., … Cui, Y. (2015). Personal thermal management by metallic nanowire-coated textile. *Nano Letters*, *15*(1), 365–371. http://doi.org/10.1021/nl5036572

[7] Liu, X., Tyler, T., Starr, T., Starr, A. F., Jokerst, N. M., & Padilla, W. J. (2011). Taming the blackbody with infrared metamaterials as selective thermal emitters. *Physical Review Letters*, *107*(4). http://doi.org/10.1103/PhysRevLett.107.045901

[8] Zhu, L., Raman, A., Wang, K. X., Anoma, M. A., & Fan, S. (2014). Radiative cooling of solar cells. *Optica*, *1*(1), 32–38. http://doi.org/10.1364/OPTICA.1.000032

[9] Rephaeli, E., Raman, A., & Fan, S. (2013). Ultrabroadband photonic structures to achieve high-performance daytime radiative cooling. *Nano Letters*, *13*(4), 1457–1461. http://doi.org/10.1021/nl4004283

[10] Zhu, L., Raman, A. P., & Fan, S. (2015). Radiative cooling of solar absorbers using a visibly transparent photonic crystal thermal blackbody. *Proceedings of the National Academy of Sciences of the United States of America*, *112*(40), 12282–12287. doi:10.1073/pnas.1509453112

[11] Raman, A. P., Anoma, M. A., Zhu, L., Rephaeli, E., & Fan, S. (2014). Passive radiative cooling below ambient air temperature under direct sunlight. *Nature*, *515*(7528), 540–4. http://doi.org/10.1038/nature13883

[12] Florides, G. A., Tassou, S. A., Kalogirou, S. A., & Wrobel, L. C. (2002). Review of solar and low energy cooling technologies for buildings. *Renewable and Sustainable Energy Reviews*. http://doi.org/10.1016/S1364-0321(02)00016-3

[13] Liou, K.-N., & Rogério dos Santos Alves; Alex Soares de Souza, E. A. (1980). *An Introduction to Atmospheric Radiation*. *International Geophysics* (Vol. 26), Page 119. http://doi.org/10.1007/s13398-014-0173-7.2

[14] Watanabe, K., Hoshino, T., Kanda, K., Haruyama, Y., & Matsui, S. (2005). Brilliant Blue Observation from a Morpho -Butterfly-Scale Quasi-Structure. *Japanese Journal of Applied Physics*, *44*(1), L48–L50. http://doi.org/10.1143/JJAP.44.L48

[15] Pris, A. D., Utturkar, Y., Surman, C., Morris, W. G., Vert, A., Zalyubovskiy, S., … Potyrailo, R. a. (2012). Towards high-speed imaging of infrared photons with bio-inspired

nanoarchitectures. *Nature Photonics*, *6*(8), 564–564. http://doi.org/10.1038/nphoton.2012.188

[16] Siddique, R. H., Diewald, S., Leuthold, J., & Hölscher, H. (2013). Theoretical and experimental analysis of the structural pattern responsible for the iridescence of Morpho butterflies. *Optics Express*, *21*(12), 14351–14361. doi:10.1364/OE.21.014351

[17] Yoshioka, S., & Kinoshita, S. (2004). Wavelength-selective and anisotropic light-diffusing scale on the wing of the Morpho butterfly. *Proceedings. Biological Sciences / The Royal Society*, *271*(August 2003), 581–587. http://doi.org/10.1098/rspb.2003.2618

[18] Kinoshita, S., Yoshioka, S., Fujii, Y., & Okamoto, N. (2002). Photophysics of structural color in the Morpho butterflies. *Forma-Tokyo-*, *17*, 103–121. Retrieved from http://sciencelinks.jp/j-east/article/200305/000020030503A0014489.php

[19] Butt, H., Yetisen, A. K., Mistry, D., Khan, S. A., Hassan, M. U., & Yun, S. H. (2016). Morpho Butterfly-Inspired Nanostructures. *Advanced Optical Materials*, 497–504. doi:10.1002/adom.201500658

[20] Potyrailo, R. A., Bonam, R. K., Hartley, J. G., Starkey, T. A., Vukusic, P., Vasudev, M., … Deng, T. (2015). Towards outperforming conventional sensor arrays with fabricated individual photonic vapour sensors inspired by Morpho butterflies. *Nature Communications*, *6*, 7959. doi:10.1038/ncomms8959

[21] Autio, G. W., & Scala, E. (1966). The normal spectral emissivity of isotropic and anisotropic materials. *Carbon*, *4*(1), 13–28. http://doi.org/10.1016/0008-6223(66)90005-4

[22] del Campo, L., Pérez-Sáez, R. B., González-Fernández, L., Esquisabel, X., Fernández, I., González-Martín, P., & Tello, M. J. (2010). Emissivity measurements on aeronautical alloys. *Journal of Alloys and Compounds*, *489*(2), 482–487. http://doi.org/10.1016/j.jallcom.2009.09.091

[23] Singham, J. (1962). Tables of emissivity of surfaces. *International Journal of Heat and Mass Transfer*, *5*(1–2), 67–76. http://doi.org/10.1016/0017-9310(62)90102-3

[24] Incropera, F. P., DeWitt, D. P., Bergman, T. L., & Lavine, A. S. (2007). *Fundamentals of Heat and Mass Transfer*. *Water* (Vol. 6th). http://doi.org/10.1016/j.applthermaleng.2011.03.022

[25] Ziman, J. M. (1960). Electrons and phonons: the theory of transport phenomena in solids. *Endeavour*. http://doi.org/10.1016/0160-9327(61)90046-1

[26] Furukawa, T., & Iuchi, T. (2000). Experimental apparatus for radiometric emissivity measurements of metals. *Review of Scientific Instruments*, *71*(7), 2843. http://doi.org/10.1063/1.1150701

[27] Richmond, J. C. (1960). Equipment and procedures for evaluation of total hemispherical emittance. American Ceramic Society bulletin, 39, 668-673.

[28] Caren, R. P. (1963). Measurement of Thermal Radiation Properties of Solids (NASA SP-31, Washington, DC, 1963). In *Measurement of Thermal Radiation Properties of Solids*.

[29] Richmond, J., De Vos, J. C. (1954). A new determination of the emissivity of tungsten ribbon. Physica, 39(7-12), 690-714.

[30] J. C. Richmond, W. N. Harrison, and F. J. Shorten (1963). Measurement of Thermal Radiation Properties of Solids (NASA SP-31, Washington, DC, 1963). In *Measurement of Thermal Radiation Properties of Solids*.

[31] Herve, P., Cedelle, J., & Negreanu, I. (2012). Infrared technique for simultaneous determination of temperature and emissivity. *Infrared Physics & Technology*, *55*(1), 1–10. http://doi.org/10.1016/j.infrared.2010.09.001

[32] Sai, H., & Kanamori, Y. (2003). Spectrally Selective Thermal Radiators and Absorbers With Periodic Microstructured Surface for High-Temperature Applications. *Microscale Thermophysical Engineering*, *7*(2), 101–115. http://doi.org/10.1080/10893950390203305

[33] Chen, K. S., & Fung, a. K. (2003). Emission of rough surfaces calculated by the integral equation method with comparison to three-dimensional moment method simulations. *IEEE Transactions on Geoscience and Remote Sensing*, *41*(1), 90–101. http://doi.org/10.1109/TGRS.2002.807587

[34] Wen, C.-D., & Mudawar, I. (2006). Modeling the effects of surface roughness on the emissivity of aluminum alloys. *International Journal of Heat and Mass Transfer*, *49*(23-24), 4279–4289. doi:10.1016/j.ijheatmasstransfer.2006.04.037

[35] DeWitt, D. P., & Incropera, F. P. (1988). Physics of Thermal Radiation. In *Theory and Practice of Radiation Thermometry* (pp. 19–89). doi:10.1002/9780470172575

[36] Modest, M. F. (2003). Radiative Properties of Real Surfaces. *Radiative Heat Transfer*, *21*(2), 125. http://doi.org/10.1177/1553350614532679

[37] Steindorfer, M. a, Schmidt, V., Belegratis, M., Stadlober, B., & Krenn, J. R. (2012). Detailed simulation of structural color generation inspired by the Morpho butterfly. *Optics Express*, *20*(19), 21485–94. doi:10.1364/OE.20.021485

[38] Huang, J., Wang, X., & Wang, Z. L. (2006). Controlled replication of butterfly wings for achieving tunable photonic properties. *Nano Letters*, *6*(10), 2325–2331. doi:10.1021/nl061851t

[39] Freihofer, G., Gupta, A., Newkirk, A. V., Seal, S., & Raghavan, S. (2014). Optical stress sensing alumina nanocomposite coatings for aerospace structures. In *AIAA SciTech, 55th AIAA/ASME/ASCE/AHS/SC structures, structural dynamics, and materials conference*. doi: 10.2514/6.2014-0159

[40] Hanning-Lee, M. A., Brady, B. B., Martin, L. R., & Syage, J. A. (1996). Ozone decomposition on alumina: Implications for solid rocket. *Geophysical Research Letters*, *23*(15), 1961–1964.

[41] Malitson, I. H., & Dodge, M. J. (1972). Refractive Index and Birefringence of Synthetic Sapphire. *J. Opt. Soc. Am.*, (62), 1405. Retrieved from https://www.osapublishing.org/DirectPDFAccess/BBB828CE-B016-D3B2-0AA95C797948DB24_171737/josa-62-11-1336.pdf?da=1&id=171737&seq=0&mobile=no

[42] Kischkat, J., Peters, S., Gruska, B., Semtsiv, M., Chashnikova, M., Klinkmüller, M., … Masselink, W. T. (2012). Mid-infrared optical properties of thin films of aluminum oxide, titanium dioxide, silicon dioxide, aluminum nitride, and silicon nitride. *Appl. Opt.*, *51*(28), 6789–6798. http://doi.org/10.1364/AO.51.006789

[43] Malitson, I. H. (1965). Interspecimen Comparison of the Refractive Index of Fused Silica. *Journal of the Optical Society of America*, *55*(10), 1205. http://doi.org/10.1364/JOSA.55.001205

[44] Stephenson, D. (1990). *Modeling variation in the refractive index of optical glasses*. Rochester Institute of Technology.

[45] Vitanov, P., Harizanova, A., Ivanova, T., Alexieva, Z., & Agostinelli, G. (2006). Deposition and Properties of the Pseudobinary Alloy (Al 2 O 3) x (TiO 2) 1- x and Its Application for Silicon Surface Passivation. *Japanese Journal of Applied Physics*, *45*(7), 5894–5901. http://doi.org/10.1143/JJAP.45.5894

[46] Choi, D., Kim, S.-J., Lee, J. H., Chung, K.-B., & Park, J.-S. (2012). A study of thin film encapsulation on polymer substrate using low temperature hybrid ZnO/Al2O3 layers atomic layer deposition. *Current Applied Physics*, *12*, S19–S23. http://doi.org/10.1016/j.cap.2012.02.012

[47] Rakić, A. D., Djurišić, A. B., Elazar, J. M., & Majewski, M. L. (1998). Optical properties of metallic films for vertical-cavity optoelectronic devices. *Appl. Opt.*, *37*(22), 5271–5283. http://doi.org/10.1364/AO.37.005271

[48] Heo, J., Liu, Y., Sinsermsuksakul, P., Li, Z., Sun, L., Noh, W., & Gordon, R. G. (2011). (Sn,Al)Ox Films Grown by Atomic Layer Deposition. *J. Phys. Chem. C*, *115*(20), 10277–10283. doi:10.1021/jp202202x

[49] Puurunen, R. L. (2014). A short history of atomic layer deposition: Tuomo Suntola's atomic layer epitaxy. *Chemical Vapor Deposition*, *20*(10-12), 332–344. http://doi.org/10.1002/cvde.201402012

[50] Coddington, O., Lean, J. L., Pilewskie, P., Snow, M., & Lindholm, D. (2015). A Solar Irradiance Climate Data Record. *Bulletin of the American Meteorological Society*, BAMS–D–14–00265.1. http://doi.org/10.1175/BAMS-D-14-00265.1

[51] Kang, S. H., Tai, T. Y., & Fang, T. H. (2010). Replication of butterfly wing microstructures using molding lithography. *Current Applied Physics*, *10*(2), 625–630. http://doi.org/10.1016/j.cap.2009.08.007